CRYSTALLIZATION IN SELF-IMPLANTED POLYCRYSTALLINE SILICON-ON-INSULATOR FILMS

by
Ralph Benhart Iverson

Bachelor of Science
Electrical Engineering and Computer Science
Massachusetts Institute of Technology
(1979)

Master of Science
Electrical Engineering and Computer Science
Massachusetts Institute of Technology
(1981)

Submitted to the
Department of Electrical Engineering and Computer Science
In Partial Fulfillment of the Requirements
For the Degree of
DOCTOR OF PHILOSOPHY
at the
MASSACHUSETTS INSTITUTE OF TECHNOLOGY
June, 1987

Signature of Author ______________________
Department of Electrical Engineering and Computer Science
May 14, 1987

Certified by ______________________
L. Rafael Reif
Thesis Supervisor

Accepted by ______________________
Chairman, Departmental Committee on Graduate Students

CRYSTALLIZATION IN SELF-IMPLANTED POLYCRYSTALLINE SILICON-ON-INSULATOR FILMS

by
Ralph B. Iverson

Submitted to the Department of Electrical Engineering and
Computer Science on May 14, 1987 in partial fulfillment
of the requirements for the Degree of Doctor of Philosophy
in Electrical Engineering and Computer Science

Abstract

This thesis investigates crystallization in polycrystalline silicon-on-insulator (SOI) films amorphized by the implantation of silicon. Polycrystalline silicon films are deposited onto an oxidized silicon wafer by low-pressure chemical-vapor deposition, implanted with silicon ions, and annealed. The crystalline fraction and grain density are measured by transmission electron microscopy as a function of implant dose, anneal time, and anneal temperature. These measurements are analyzed to determine the crystallization parameters of implanted polycrystalline SOI.

At low implant doses, the films are nearly amorphous; but enough crystalline material is left that the subsequent anneal reproduces the morphology of the as-deposited films. As the dose is increased, fewer grains survive; and the grains in implanted and annealed films are larger than in the as-deposited films. At still higher doses (the "channeling regime"), only grains which exhibit ion channeling survive; and the annealed films have larger grains and are textured as well. At large doses (complete amorphization) the final grain size saturates at 1–2 μm. The crystallization behavior at complete amorphization indicates that the final grain size is dictated by steady-state nucleation and growth rates after a transient time. The transient period is the time necessary to produce a steady-state cluster (microcrystal) population, which is a prerequisite to steady-state nucleation. The nucleation rate for doses between the channeling regime and complete amorphization is a strong function of implant dose. This is attributed to a population of clusters which is eradicated as the implantation dose is increased. This population is extinct at complete amorphization.

Thesis Supervisor: Dr. L. Rafael Reif
Title: Associate Professor of Electrical Engineering

Acknowledgements

My foremost thanks go to my thesis committee, whose guidance has been instrumental in completing this work: my thesis advisor Professor Rafael Reif; and my thesis readers, Professors Dimitri A. Antoniadis and Henry I. Smith. I would also like to extend my thanks to several other deserving individuals: Harry Atwater and Prof. Carl V. Thompson for information about crystallization processes; Mark Rodder for information concerning TFT's; Mike Frongillo and Gabriella Chapman for help with TEM; Tri-Rung Yew for cross-sectional TEM work; Carolyn Zaccaria for administrative services; and numerous friends, whom I have burdened at times with thesis woes. I would also like to acknowledge the Mandala Folk Dance Ensemble for the regular relief from academia that it has provided me.

I thank my parents, Ben and Ida, for their support. Finally, for the support she has always given me whether I needed it or not, I would like to express my gratitude to my wife Pat; though, I am more grateful than words can say.

This work was supported by the National Science Foundation (Grant No. 83-03450ECS) and the MIT Center for Materials Science and Engineering (NSF-MRL Grant No. DMR84-18718).

Contents

List of Figures

List of Symbols

α	Amorphous fraction.
$\Gamma(p)$	Gamma function, $\int_0^\infty x^{p-1}e^{-x}\mathrm{d}x$.
ΔG_n	Free energy of formation of a cluster size n.
ΔG_n^*	Maximum free energy of formation of a cluster.
ΔG_{a-x}	Gibbs free energy difference between amorphous and crystalline phases (energy/atom).
ΔG_{surf}	Interfacial energy (energy/surface atom).
ϵ	Film thickness.
ν	Jump frequency of an atom at a phase interface.
ρ_g	Density of grains (#/area).
ρ_n	Density of nucleated grains (#/area).
ρ_s	Density of seed grains (#/area).
σ_{ρ_g}	Standard deviation of measured grain density.
σ_χ	Standard deviation of measured crystalline fraction.
τ_0	Transient time.
τ_n	Characteristic crystallization time for nucleated crystallization (constant nucleation rate).
τ_s	Characteristic crystallization time for seeded crystallization.
χ	Crystalline fraction.
χ_n	Crystalline fraction due to nucleated crystallization.
χ_s	Crystalline fraction due to seeded crystallization.

A_D	Effective ion-damage area.
A_D^C	Effective ion-damage area in oriented grains.
A_G	Grain area in annealed film.
A_G^{dep}	Grain area in as-deposited film.
$A_{G,n}$	Final grain area due to steady-state nucleation.
$A_{G,s}$	Final grain area due to seeded crystallization.
E_d	Activation energy of interstitial self-diffusion in silicon.
E_{r_n}	Activation energy of nucleation rate r_n.
E_{τ_0}	Activation energy of transient time τ_0.
E_{v_g}	Activation energy of growth rate v_g.
f_c	Fraction of grains in a channeling orientation.
f_d	Dechanneling fraction of ions in oriented grains.
k^*	Reaction rate at critical cluster size.
$k_{n\rightarrow n+1}$	Forward reaction rate of cluster size n.
$k_{n+1\rightarrow n}$	Reverse reaction rate of cluster size $n+1$.
k	Boltzman constant.
n	Cluster size.
n^*	Critical cluster size.
N_n	Number of clusters of size n.
P_C	Implant survival probability of a cluster.
P_G	Implant survival probability of a grain.
P_G^C	Implant survival probability of an oriented grain.
P_G^R	Implant survival probability of a randomly-oriented grain.
Q	Implant dose (# ions/area).
Q_C	Channeling dose offset (# ions/area).
r_n	Steady-state nucleation rate (# grains/volume-time).
t	Time.
T	Absolute temperature.
v_g	Growth rate (velocity).

Chapter 1

Introduction

This thesis investigates crystallization in polycrystalline silicon-on-insulator (SOI) films amorphized by the implantation of silicon. The crystallization process determines grain size which has a large effect on the electrical properties of the film and, consequently, on the characteristics of thin-film transistors (TFT's) well.

Silicon-on-insulator technology has become a subject of great interest and several techniques of film preparation have been investigated.[1–9] Some techniques involve the melting of a deposited film: laser recrystallization of polycrystalline silicon;[1] lateral epitaxial growth from seeding windows by melting;[2] and graphoepitaxy using a laser[3] or strip-heater oven[4] as a heat source. Other methods operate at lower temperatures, utilizing solid-phase processes: lateral solid-phase epitaxy;[5,6] seed selection through ion channeling (SSIC);[7,8] and secondary grain growth.[9]

A layer of low-defect single-crystal SOI would expand the capabilities of VLSI enormously. Thin film transistors built in high-quality SOI would result in larger packing densities leading to larger memories, faster circuits, and smaller chip sizes. The additional fabrication steps, however, increase the cost per wafer while decreasing yield.

The high processing temperature required by some SOI technologies cannot be combined with current VLSI processes because of the dopant diffusion and thermal stress it would cause. VLSI fabrication is more easily adapted to the lower-temperature SOI technologies which use solid-phase crystallization processes. In this regime, lateral solid-phase epitaxy probably produces the highest-quality SOI. It does, however, require seed windows and therefore poses some restrictions on VLSI layout. Also, the lateral growth distance is only on the order of 5 μm for undoped films.[5] (A growth distance of 24 μm was achieved[6] with 3×10^{20} phosphorus atoms/cm^3, but such material would be useful only as a conductor.)

Silicon-on-insulator applications other than VLSI are also attractive. SOI could be used to build devices and circuits on various substrates: on transparent substrates for flat-panel displays; on inexpensive substrates for solar-cells; and on different semiconductor materials for hybrid monolithic integration. Novel devices using SOI can also be envisioned.

Functional thin film transistors do not require a single-crystal layer of silicon, though the channel mobilities do correlate with the crystallinity. In fact, TFT's have been fabricated on amorphous as well as polycrystalline silicon films.[10–12]

Amorphous TFT technology has an advantage of lower processing temperatures than for polycrystalline silicon films. Channel mobilities of TFT's on amorphous silicon,[10] unfortunately, are quite low: less than 1 cm^2/V·sec for electrons.

In polycrystalline silicon films deposited by chemical-vapor deposition (CVD), the morphology is a function of film thickness. Thin films contain small grains. Thick films consist of a bottom layer of small grains with the remainder containing columnar grains. In all cases, the grain size is less than the film thickness. A 5000Å layer of polycrystalline silicon deposited by low-pressure chemical-vapor deposition (LPCVD) has a grain size[13] between 500Å and 900Å. The channel mobility in TFT's built on polycrystalline silicon is higher than for amorphous silicon, but lower than for single-crystal MOSFET's because of grain-boundary effects. One method of reducing grain-boundary effects is by hydrogen passivation.[14] Another is by reducing the number of grain boundaries (larger grain size). In small-grain polysilicon,[11] the channel mobility is on the order of 10 $cm^2/V{\cdot}sec$ for electrons.

Larger grain size can be produced by first amorphizing the polycrystalline film by implantation and then recrystallizing it by a low-temperature anneal (550°C–700°C).[8,15,16] In such a procedure, grain size of a few microns can be achieved. Recently, TFT's built on films prepared in this way[12] had a channel mobility of more than 100 $cm^2/V{\cdot}sec$ for electrons.

The goal of this thesis is to characterize the crystallization behavior of self-implanted polycrystalline silicon films, providing an understanding of how two major parameters (implant dose and anneal temperature) affect the texture and grain size in implanted and annealed films.

Ion implantation amorphizes a polycrystalline film according to the dose. As the dose is increased, more grains are amorphized. Certain crystal orientations (relative to the implant direction) are harder to amorphize due to ion channeling[17] — when the ion path is coincident with an axis or plane of high symmetry, the ion travels between the rows or planes of atoms and causes little damage. Because of the channeling effect, orientation effects should be apparent over a range of doses (called the "dose-window") where "oriented" grains survive the implant and other (randomly-oriented) grains are amorphized. These oriented grains serve as seeds in a subsequent anneal. This process is called "seed selection through ion channeling", or SSIC.

The post-implant anneal crystallizes the film. Any grains that survive the implant will grow until they impinge upon one another. When there are no surviving grains, crystallization is from grains which nucleate spontaneously.

Models of the amorphization and crystallization processes are derived in Chapter 2. Amorphization is a function of the implant dose. (The ion energy and target temperature are also factors, but they are not varied in this thesis.) Classical nucleation theory (atomic scale) is presented. Crystallization in thin implanted films (microscopic scale) is then considered from two sources: from existing seed crystals (hereafter referred to as *seeded* crystallization); and from nucleated crystallites (hereafter referred as *spontaneous* or *nucleated* crystallization).

Chapter 3 explains the experimental methods common to the experiments presented here (Chapters 4-7): film growth; implantation; furnace anneal; preparation for transmission electron microscopy; and collection of data, including error estimation. Also, the morphology of the as-deposited film is described.

The experiments presented here (by chapter) are:

4. **Dose Dependence of Final Grain Size in Amorphized and Recrystallized Polycrystalline Silicon Films.**[18] This experiment involves several samples of polycrystalline silicon. Each is implanted with silicon. The dose is varied from 1×10^{14} to 5×10^{15} ions/cm^2 in order to produce a different degree of amorphization in each sample. The samples are then completely recrystallized by a low-temperature anneal. The experimental results (final grain size as a function of implant dose) are compared with a model (from Chapter 2) which accounts for channeling effects. Also included and providing further evidence of the channeling effect are the results of related experiments by Kung *et al.*[19–21] using X-ray pole-figure analysis to investigate the {110} texture of implanted and annealed films.

5. **Temperature Dependence of Crystallization Parameters in Silicon Films Amorphized by Implantation.**[23] In this experiment, several polycrystalline silicon films are implanted with 5×10^{15} ions/cm^2, enough to destroy virtually all seed crystallites. At each of five temperatures (580°C, 590°C, 600°C, 630°C, and 640°C), crystallization parameters are determined from the collected data (density of grains ρ_g versus anneal time, and amorphous fraction χ versus anneal time). Activation energies are then determined, based on the calculated parameters at the five anneal temperatures. The activation energies determine some of the thermodynamic parameters used in classical crystallization theory (Chapter 2).

6. **Crystallization in a "Seeded" Amorphous Film.**[22] In this experiment, a polycrystalline silicon film is implanted with 2×10^{15} ions/cm^2. This dose is selected to produce an amorphous film with approximately 25 grains/μm^2. The film is then annealed at 580°C for varying lengths of time. The density of crystallites and the crystalline fraction (as a function of anneal time) indicate that the source of crystallization is probably due to microcrystals, not due to seed grains as originally presumed. (Crystallization was originally thought to be due to seed grains since nucleation in amorphous silicon produces less than one grain per square micron.)

7. **Dose Dependence of Crystallization Parameters in Silicon Films Amorphized by Implantation.**[24] This final experiment shows how the crystallization parameters vary with implant dose. Three doses are used: 4×10^{15}, 5×10^{15}, and 6×10^{15} ions/cm^2. The parameters are determined at 630°C. These results are combined with data from the previous experiments to provide a global picture of the effect of implant dose on crystallization.

Chapter 8 reviews the theoretical and experimental results of this work and includes several suggestions for future work.

Chapter 2

Theory of Implantation Damage and Subsequent Crystallization

2.1 Introduction

This chapter contains the theory which served as the original hypothesis of this work: the effect of implantation on the structure of polycrystalline silicon, the classical theory of nucleation and growth, and the crystallization behavior of films from seed grains and from nucleated grains.

The effects of implantation on crystallinity in single-crystal silicon have been investigated intensively[25–32] and are fairly well described. In this chapter, implantation effects are extended theoretically into the domain of polycrystalline films. The theory is presented here as it was hypothesized before any experimental confirmation. A modification indicated by subsequent data (Chapters 4–7) is outlined in the concluding section of this chapter.

The classical theory of nucleation and growth provides the theoretical background necessary for understanding crystallization processes on an atomic scale, where implantation effects are manifested.

Crystallization is analyzed on a microscopic scale because data are collected on the microscopic scale. Density of grains $\rho_g(t)$ and crystalline fraction $\chi(t)$ are the two quantities measured to determine the crystallization parameters. Crystallization of polycrystalline films is assumed here to arise from two sources: the growth of seed grains; and/or the growth of grains nucleating at a steady-state rate. Given a constant growth velocity v_g and either an initial density of seeds ρ_s or a constant nucleation rate r_n, crystallization becomes a geometrical problem. This was first treated by Johnson and Mehl[33] and by Avrami.[34-36] One other crystallization parameter, τ_0 is also used — it is the initial transient time, during which little nucleation occurs. The measurements used in this thesis are: the crystalline fraction $\chi(t)$ and the density of grains $\rho_g(t)$ in partially annealed films; and final grain size A_G in 100% recrystallized films. These quantities are derived here in terms of the crystallization parameters (v_g, r_n, ρ_s, and τ_0) which, in turn, are found in terms of some thermodynamic parameters used in classical nucleation theory. In later chapters, the crystallization parameters v_g, r_n, ρ_s, and τ_0 are extracted from the crystallization data ($\chi(t)$, $\rho_g(t)$, and A_G) using the theory developed in this chapter. From v_g, r_n, ρ_s, and τ_0, thermodynamic parameters of the classical nucleation theory are found.

2.2 Implantation Damage in Polycrystalline Material

In this section, the model of implantation damage in polycrystalline silicon is developed. Ion implantation damage is first described in a crystalline material. Then the basic model is developed. This theory treats the impact positions of the ions as *random* on an atomic scale, as opposed to *uniform* on a microscopic scale. Ion channeling is then described and its effects are included in the model.

2.2.1 Ion Implantation

When a high-energy ion enters a target, it loses energy through coulombic interactions with electrons and with target nuclei. Because electrons are much lighter than ions, each interaction is small. The cumulative effect, therefore, is to uniformly slow any incident ion. The trajectory can be greatly influenced, however, by interactions with target nuclei, depending on the relative masses. These interactions are usually analyzed to determine the implant profile (the position profile of the final ion positions).

The ion energy transferred through collisions with the nuclei is called "damage energy" since an ion-nucleus interaction can impart enough energy to a target nucleus to displace it. (In fact, the energy transferred can be high enough that the displaced nucleus needs to be treated as a secondary energetic ion in detailed damage-energy calculations.[37,38]) In a crystalline material, implantation produces a degree of amorphization which depends on the implant dose. Since all energy lost is ultimately manifested as heat, it is also possible for some self-annealing to occur. To minimize heating during an implant, therefore, low implant current and/or reasonable heat-sinking is required.

To first order, the amorphization (lattice damage) caused by a beam of high-energy ions is proportional to the damage energy which, in turn, is proportional to the ion dose. This model has been used to calculate the amorphization dose as a function of energy. A critical damage energy for single-crystal silicon of 12 eV/atom has been determined by Narayan *et al.*[32] Assuming damage is uniform and the depth of the damage is known, the dose required to amorphize a layer of silicon can be easily found. The value of 12 eV/atom, it should be noted, is not the energy required to knock a silicon atom out of its lattice position. It is no more than the *average* damage energy per atom that needs to be deposited to ensure that no significant crystalline areas remain.

The assumption that the amorphization damage is proportional to dose is adequate in some cases. The paper by Narayan *et al.*, however, also shows that the amorphous region contains microcrystallites. This is because on the atomic scale the ion trajectories are random (*not* uniform); some small volumes are less damaged than others. If an implanted layer is being regrown epitaxially, the microcrystallites (which are of the same orientation as the substrate) have little or no effect. In amorphized polycrystalline silicon on oxide, however, these microcrystallites are of major importance since they may serve as seeds in the absence of a seeding substrate.

In 1981, Komem and Hall[15] reported a dose dependence of the final grain size in polycrystalline silicon films which were implanted with germanium and annealed. They found that an annealed film which was implanted with a dose of 2×10^{15} ions/cm^2 was similar to the as-deposited film; however, as-annealed film which was implanted with a dose of 4×10^{16} ions/cm^2 consisted of large (over 1 μm) dendritic grains, about 10 times larger than in the as-deposited film. By transmission electron microscopy (TEM), the two as-implanted films were amorphous — there were no observable differences in crystallinity. The ability of the low-dose sample to recover its original morphology was attributed to "memory" of grain boundaries — it was suggested that at a sufficiently small dose, the grain boundaries survive and block crystallization. In this work, the memory effect is attributed to microcrystallites rather than to grain-boundary memory.

2.2.2 Survival Probability of Grains in Polycrystalline Material

The implant dose controls the degree of amorphization of a polycrystalline film. On an atomic scale, the impact positions of the ions are random (*not* uniform). This means that at a given dose, grains may survive the implant due to chance — either few ions may hit a grain or those that hit may be more concentrated than average, leaving some part or parts of the grain relatively undamaged. The model developed here assumes that upon implantation, each grain is in one of two states: a grain may be completely amorphized; or enough crystalline structure survives to serve as a seed in a subsequent anneal. The trace crystallinity in as-implanted films is too small to be measured by conventional methods like transmission electron microscopy (TEM) or Rutherford back-scattering (RBS). In Chapter 4, the probability that a grain survives the implant, P_G is found experimentally by recrystallizing the film at a low temperatures (700°C) and determining the average final grain size: $A_G = A_G^{dep}/P_G$. This assumes that (1) there is no spontaneous nucleation and (2) each surviving grain results in only one seed (multiple crystalline regions within a single grain "unite" upon annealing). The first assumption is accounted for later in this chapter. The second, however, is maintained throughout this work in view of the ability of epitaxial regrowth to reclaim microcrystals in the amorphized layer of single-crystal silicon, as noted above.

In addition to treating the impact positions as random rather than uniform, the volume of damage associated with each ion is modeled as an effective area A_D which depends on the implant parameters (ion energy, ion-target combination, and target temperature). This is an *effective* area because crystal structure may survive at any depth. Moreover, this is an *average* effective area because the cascades (paths of primary and secondary ions) due to identical ions may vary significantly. At high energies, a primary ion displaces target nuclei at large irregular intervals. At low energies, the damage is more dense.

The probability of a grain surviving an implant is analogous to the probability that a tile in a room is not completely covered when one tosses in a large number of coins. In this analogy, the tile represents a grain of polycrystalline silicon and each coin represents the damage caused by a single ion. This problem has two parameters (A_G^{dep} and A_D) and one variable, the dose Q (represented in the analogy by the number of coins per unit area) and is solved in Appendix A. The solution is written here as

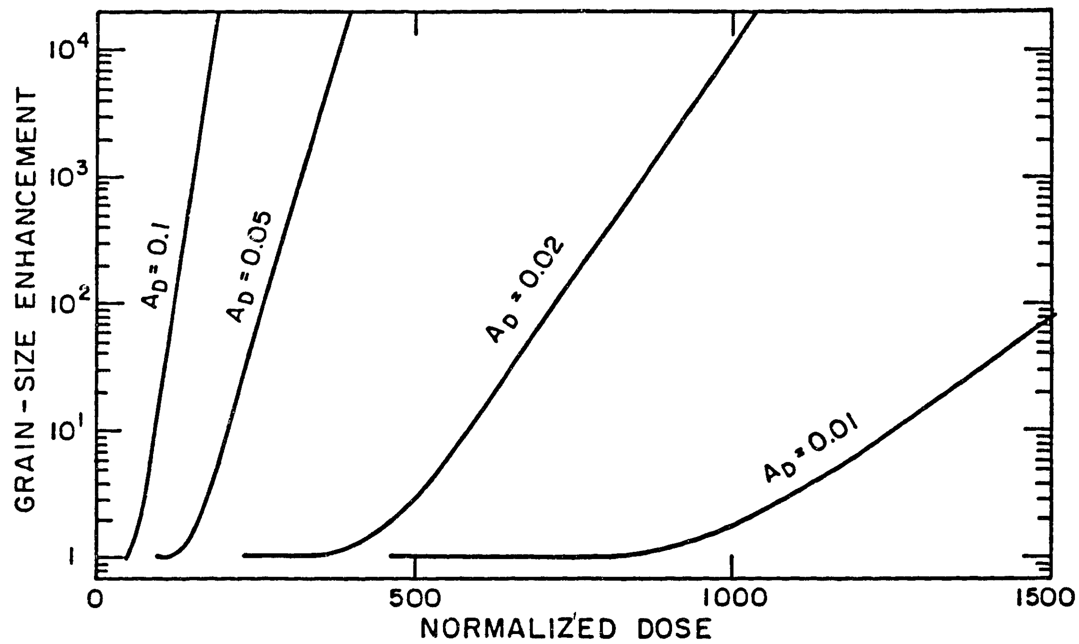

Figure 2.1: Normalized final grain size versus normalized implant dose for several values of normalized damage area A_D based on Eqn. (2.1). All quantities are normalized to the initial grain size A_G^{dep}.

$$-\ln(1 - P_G^R) = 2Q^2 A_G^{dep} A_D \exp(-QA_D) \tag{2.1}$$

and is valid for $QA_D > 4.6$. The superscript on P_G denotes that this is the survival probability in the absence of channeling — as described further on, damage in grains which exhibit channeling effects is modeled by modifications to Eqn. (2.1). Figure 2.1 shows a theoretical plot of the normalized final grain size versus normalized implant dose with all areas normalized to A_G^{dep}— the dose Q is in units of ions/A_G^{dep}, and A_D is unitless.

2.2.3 Ion Channeling

Implantation damage is a function of dose, ion species, and implant energy. In crystals, it is also a function of the implant angle. When the path of the ion is nearly parallel to a high-symmetry axis of the crystal, the ion usually channels (passes between rows of atoms); as the ion nears any row of atoms, the cumulative interaction with the row deflects it away even though the interaction with each nucleus in the row is small. Little damage occurs in this case and the trajectory of the ion is straight and much longer than in a random (non-channeling) direction.[39–48] The orientation-sensitivity of amorphization was shown dramatically by Nelson and Mazey[17] who implanted {100}, {110}, and {111} silicon wafers from a point source at close proximity. Each position on a wafer, therefore, corresponded to implantation in a particular crystallographic direction. The degree of amorphization in these wafers could be qualitatively determined optically. All major planes and axes exhibited less amorphization than other (random) directions. Other research of channeling damage has also been done,[44–46] but none demonstrate the effect in such a visual form. The major channeling direction is <110>, as is suggested in Fig. 2.2, which shows perspective views of silicon along <100>, <110>, and <111> channels.

2.2.4 Channeling Effects in Polycrystalline Silicon

Channeling also occurs in polycrystalline silicon, but only in properly oriented grains. Channeling through polycrystalline silicon was reported in 1979 by Seidel.[47] When implantation was used to phosphorus-dope the

(a) <100>

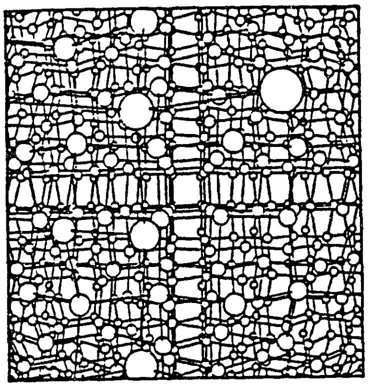

(b) <110>

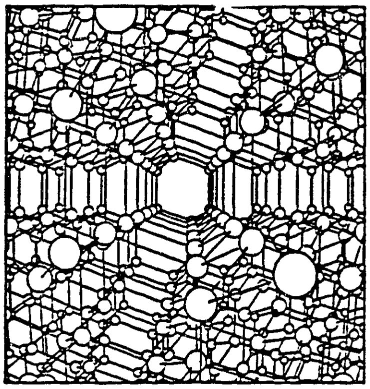

(c) <111>

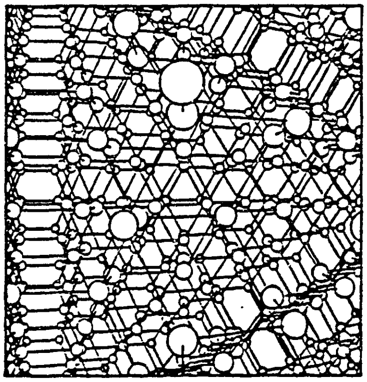

Figure 2.2: Perspective views of silicon along the (a) <100>, (b) <110>, and (c) <111> channels.

polycrystalline silicon gate of an NMOS enhancement-mode transistor, it became a depletion-mode device, even though the implant depth was less than the gate thickness. This effect was eliminated by any of three methods: amorphization of the top of the gate material; thermal oxidation of the top of the gate material; or reduction of the implant energy.

A novel low-temperature SOI process, proposed in 1981 by Reif and Knott,[48] utilizes the orientation-dependence of implant damage to selectively amorphize polycrystalline silicon:

1. Deposit polycrystalline silicon on a thermally oxidized wafer. However, any non-seeding substrate able to withstand 625°C (deposition temperature of the silicon film) is suitable.
2. Implant with enough silicon ions to amorphize the film only where no channeling occurs. By implanting from appropriate angles, only grains of one orientation should survive. Hereafter, these grains are called "oriented grains", meaning that they are oriented with respect to the ion beam such that the ions channel. Other grains are called "randomly-oriented grains". This step is called "seed selection by ion channeling", or SSIC.
3. Anneal at a low temperature to crystallize using the surviving grains to seed the film.

The implant dose must fall within a range of values called the "dose window": if the dose is too small, grains of random orientations survive the implant; or if the dose is too large, all the grains are amorphized.

The dose window should be apparent from a plot of final grain size as a function of implant dose — within the dose window, the final grain size should be larger than the as-deposited grain size, and yet it should be only a weak function of dose. Equation (2.1) can be modified to include grains which exhibit channeling. The forms used here assume that a fraction f_c of the as-deposited grains exhibit channeling effects and that the same degree of channeling occurs in each of these grains. This is a simplification of what is actually expected because different orientations support different degrees of channeling.

Three models are considered here for the survival probability, P_G^C, of an oriented grain:

1. Assume implantation damage is negligible below a critical ion dose Q_C (so that $P_G^C = 1$) and that above Q_C the damage is the same as for randomly-oriented grains. For oriented grains, survival probability is found at doses above Q_C by substituting $(Q - Q_C)$ in place of Q in Eqn. (2.1):

$$-\ln(1 - P_G^C) = 2(Q - Q_C)^2 A_G^{dep} A_D \exp\left[-(Q - Q_C)A_D\right] \quad (2.2)$$

2. Assume that implantation damage is due to a dechanneling fraction f_d of ions. The survival probability is found by substituting $f_d Q$ in place of Q in Eqn. (2.1):

$$-\ln(1 - P_G^C) = 2{f_d}^2 Q^2 A_G^{dep} A_D \exp(-f_d Q A_D) \quad (2.3)$$

3. Assume that the volume and magnitude of ion damage in oriented grains can be treated in a manner similar to damage in random grains.

In this case, the survival probability is found by using a smaller effective damage area A_D^C in place of A_D in Eqn. (2.1):

$$-\ln\left(1 - P_G^C\right) = 2Q^2 A_G^{dep} A_D^C \exp\left(-QA_D\right) \tag{2.4}$$

2.2.5 Density of seeds

The density of seeds ρ_s in an implanted polycrystalline silicon film is the sum of the density of randomly-oriented surviving grains and oriented surviving grains:

$$\rho_s = \left[(1 - fc)P_G^R + (fc)P_G^C\right] / A_G^{dep}, \tag{2.5}$$

where f_c is the fraction of grains that exhibit channeling effects. The survival probability of a randomly-oriented grain, P_G^R, is calculated by Eqn. (2.1). The survival probability of an oriented grain, P_G^C, is calculated by one of three modifications to Eqn. (2.1): Eqn. (2.2), (2.3), or (2.4).

In the absence of nucleation, the grain size upon crystallization is $A_{G,s} = 1/\rho_s$. From the theory presented so far, two plateaus should be observable in a plot of final grain size A_G versus implant dose Q: at low doses, few grains (oriented *or* randomly-oriented) are amorphized completely so that $A_G \approx A_G^{dep}$; and within the dose window, most randomly-oriented grains are completely amorphized though few oriented grains are so that $A_G \approx A_G^{dep}/f_c$.

2.3 Crystallization

Nucleation during crystallization affects the grain size and texture of the annealed film. Since nucleation increases the density of crystallites, the final grain size is smaller than indicated by Eqn. (2.5). Furthermore, nucleated grains are not expected to conform to the orientation selectivity of ion channeling within the dose window. The following sections describe the classical theory of nucleation and growth, crystallization due to a steady-state nucleation rate, crystallization from seed grains, and crystallization from a combination of seed grains and nucleated grains. The nomenclature used here is loosely based on the nomenclature in a paper by Kelton *et al.*[49] on transient nucleation.

2.3.1 Parameters of nucleation theory and crystallization behavior

The parameters used here can be divided into two sets: parameters which are used with thermodynamics to describe crystallization on an atomic level; and the crystallization parameters which are more directly measured, such as growth velocity, nucleation rate, and characteristic crystallization time.

The three energies used here to describe crystallization on an atomic level are:

- The difference (per atom) in Gibb's free energy between the amorphous and crystalline phases (ΔG_{a-x});
- The energy required (per interface atom) to maintain an interface between the two phases (ΔG_{surf}); and
- The activation energy E_d associated with the unbiased jump frequency ν of an atom at the interface. (The unbiased frequency is

the frequency at which an interfacial atom would change phases given that there is no net change in energy.)

As shown in this chapter, these three energies are related to the temperature-dependence of the "microscopic-scale" parameters of crystallization:

- A growth velocity v_g, which is assumed to be time-independent;
- An initial transient period τ_0, during which no nucleation occurs; and,
- A steady-state nucleation rate r_n starting at time $t = \tau_0$.

(There are also characteristic times of crystallization for growth from seed grains, τ_s, or from nucleated grains, τ_n, but these can be described as functions of v_g, r_n, and the initial seed density ρ_s.)

2.3.2 Classical theory of nucleation and growth

The classical theory of nucleation and growth postulates the existence of crystalline clusters so small that they are unstable, tending to shrink because the energy required to maintain the crystalline-amorphous interface outweighs the Gibb's free-energy difference between the crystalline and amorphous phases.

Consider an amorphous medium with no clusters. With time, the system tries to reach thermodynamic equilibrium, for which the relative populations (by cluster size n) of clusters can be easily determined from the total free energy of formation (*interfacial energy – phase energy difference*). Since the interfacial energy is proportional to the surface area (radius squared) and the energy difference between the phases is proportional to the volume (radius cubed), clusters larger than a critical size n^* *grow* to minimize the free-energy of the system. In other words, the system cannot reach a thermodynamic equilibrium cluster population in an amorphous medium — the "super-critical" clusters grow until the system is crystalline. The system can, however, approach steady-state *within the amorphous fraction*, in which one can observe a steady-state nucleation rate (per amorphous volume), even though the amorphous fraction decreases with time.

According to classical theory, microcrystallites (containing only a few atoms) nucleate frequently. Because of a large surface-to-volume ratio these tend to shrink. From thermodynamic considerations, however, a few become large enough that further growth is energetically favorable. Growth in the microcrystalline regime occurs by the same basic mechanism as growth in the "macrocrystalline" regime: the rate at which each atom at an amorphous-crystalline interface makes a transition between the amorphous state and the crystalline state is a function of the energy levels of the two states. Growth is energetically favorable when the free energy of the system is lowered by the transition of an interface atom from the amorphous to the crystalline states.

The free energy of formation ΔG_n of a cluster of size n consists of two components: the Gibbs free energy difference between crystalline and amorphous phases (proportional to volume, or n); and the energy required to maintain the amorphous-crystalline interface atom (proportional to surface area, or $n^{2/3}$). The Gibbs free energy difference between the amorphous and crystalline phases is denoted here as ΔG_{a-x} and is in units of eV/atom. It is taken to be positive. That is, the energy of each atom in the cluster is lower than the energy of an atom in the amorphous phase by ΔG_{a-x}. The interfacial energy is denoted here as ΔG_{surf} and is in units of eV/surface atom.

The free energy of formation of a cluster size n may be written

$$\Delta G_n = Cn^{2/3}\Delta G_{surf} - n\Delta G_{a-x}, \tag{2.6}$$

where C is a geometrical parameter related to the the shape of the cluster. At small cluster sizes, the interfacial energy outweighs the energy difference due to the phase change — the net free energy of formation ΔG_n is positive. The maximum free energy of formation, denoted ΔG_n^*, can be found from Eqn. (2.6) and occurs at what is called the critical cluster size, n^*. This energy enters into the temperature dependence of the steady-state nucleation rate r_n.

The forward reaction rate $k_{n\rightarrow n+1}$ is the rate that a cluster grows from n to n+1 atoms. The reverse reaction rate $k_{n+1\rightarrow n}$ is the rate that a cluster shrinks from n+1 to n atoms. These rates are found by defining an unbiased atomic jump frequency ν at the amorphous-crystalline interface. Since ν is probably closely related to the jump rate in the amorphous phase, it can be characterized by the activation energy, E_d, of self-diffusion in amorphous silicon:

$$\nu \propto \exp\left(-E_d/kT\right). \tag{2.7}$$

Since all reaction rates are proportional to ν, E_d enters into the activation energies for transient time τ_0, steady-state nucleation rate r_n and growth velocity v_g.

The reaction rates are also proportional to the number of atoms at the cluster surface and may be written in the following form:

$$\begin{aligned} k_{n\to n+1} &\propto n^{2/3}\exp\left(-E_d/kT\right)\exp\left[(\Delta G_{n+1}-\Delta G_n)/2kT\right], \text{ and} \\ k_{n+1\to n} &\propto n^{2/3}\exp\left(-E_d/kT\right)\exp\left[(\Delta G_n-\Delta G_{n+1})/2kT\right]. \end{aligned} \tag{2.8}$$

A complete analysis of the reaction rates (Eqn. (2.8)) and ΔG_n (Eqn. (2.6)) provides values for the crystallization parameters transient time, nucleation rate, and growth velocity within the scope of classical theory. The activation energies of the crystallization parameters, as shown below, are related to ΔG_n^*, ΔG_{a-x}, and E_d. The transient time is the effective time to reach a steady-state nucleation rate from the initial conditions (no clusters). At steady-state, the number of clusters N_n of each cluster size n is time-independent and the net forward reaction rate $(N_n k_{n\to n+1} - N_{n+1}k_{n+1\to n})$ is equal to the steady-state nucleation rate r_n for all n. Growth velocity is found from the net forward reaction rate for a large cluster.

2.3.3 Transient nucleation time

A number of analyses of transient nucleation have been published.[50–54] In each case, a characteristic time τ_t associated with transient nucleation was found to have the same temperature dependence. Assuming that the free energy of formation is a weak function of temperature, the form is

$$\tau_t \propto T/k^*, \tag{2.9}$$

where k^* is the forward (or reverse) reaction rate at the critical cluster size. From Eqn. (2.8),

$$k^* \propto n^{*2/3} \exp(-E_d/kT). \tag{2.10}$$

Kashchiev's theoretical results,[54] which are in good agreement with experiment, indicate that the transient time τ_0 is proportional to τ_t, so that

$$\tau_0 \propto T \exp(E_d/kT). \tag{2.11}$$

The linear temperature term in Eqn. (2.11) contributes kT to E_{τ_0} (defined here as the slope of τ_0 on an Arrhenius plot):

$$\begin{aligned} E_{\tau_0} &= \frac{\mathrm{d}\ln(\tau_0)}{\mathrm{d}(1/kT)} \\ &= E_d - kT. \end{aligned} \tag{2.12}$$

Since Eqn. (2.11) does not have a true Arrhenius form, E_{τ_0} in Eqn. (2.12) is not a true activation energy. For the anneal temperatures used in this thesis, however, kT varies only slightly around 0.075 eV. The Arrhenius form is taken here to be $\exp(E/kT)$ for times (τ_0 and τ_n) and $\exp(-E/kT)$ for rates (r_n and v_g)

2.3.4 Nucleation rate

The theoretical temperature dependence of the steady-state nucleation rate[49] is

$$r_n \propto \frac{1}{T} \exp[-(E_d + \Delta G_n^*)/kT]. \tag{2.13}$$

The product of Eqns. (2.11) and (2.13) is:

$$\tau_0 r_n = \exp(-\Delta G_n^*/kT) \tag{2.14}$$

and the maximum free energy of formation of a cluster can be written as

$$\Delta G_n^* = E_{r_n} - E_{\tau_0}, \tag{2.15}$$

where E_{r_n} is the absolute slope of r_n on an Arrhenius plot.

2.3.5 Growth rate

The growth rate can be found from the net forward reaction rate for a large cluster. Addition of one atom to a large cluster does not significantly change the surface energy. The change in free energy, then, is $-\Delta G_{a-x}$. From Eqn. (2.8), assuming $\Delta G_{a-x} \gg 2kT$,

$$\begin{aligned}\frac{\mathrm{d}n}{\mathrm{d}t} &= k_{n\to n+1} - k_{n+1\to n} \\ &\propto n^{2/3}\exp\left(-E_d/kT\right) \times \\ &\quad \left[\exp\left(\Delta G_{a-x}/2kT\right) - \exp\left(-\Delta G_{a-x}/2kT\right)\right] \\ &\propto n^{2/3}\exp\left[-(E_d - \Delta G_{a-x}/2)/kT\right]. \end{aligned} \tag{2.16}$$

Because n is proportional to the radius cubed (r^3), Eqn. (2.16) is easily solved for v_g ($= \mathrm{d}r/\mathrm{d}t$):

$$v_g \propto \exp\left[-(E_d - \Delta G_{a-x}/2)/kT\right]. \tag{2.17}$$

The Gibbs free energy difference between the amorphous and crystalline phases, therefore, is:

$$\Delta G_{a-x} = 2(E_{v_g} - E_d), \tag{2.18}$$

where E_{v_g} is the activation energy of the growth velocity.

2.3.6 Crystallization due to nucleation

Crystallization due to nucleation of grains is analyzed in Appendix B using steady-state nucleation and growth rates. Whereas the nucleation rate is initially zero (assuming no clusters initially) and rises during a transient period towards a steady-state value, we assume here that this can be reasonably modeled by no nucleation during an effective transient time τ_0 and a steady-state nucleation rate r_n thereafter. This can be represented by a shift of the time axis: $t \rightarrow t - \tau_0$.

From Eqn. (B.6) the crystalline fraction in a film of thickness ϵ as a function of anneal time becomes

$$\chi_n(t) = 1 - \exp\left\{-[(t-\tau_0)/\tau_n]^3\right\} \tag{2.19}$$

where τ_n is the characteristic crystallization time due to nucleation and is given by

$$\tau_n = 1/\sqrt[3]{\tfrac{\pi}{3} v_g{}^2 \epsilon r_n} \, . \tag{2.20}$$

The density of grains (from Eqn. (B.10)) is still

$$\rho_n(t) = \epsilon r_n \tau_n \, g(u), \tag{2.21}$$

but the normalized time parameter u is now redefined as $(t - \tau_0)/\tau_n$. The function $g(u)$ is defined in Eqn. (B.9). For $t \ll \tau_n$, $g(u) \approx u$ and the density of grains is linear in time: $\rho_n(t) = \epsilon r_n (t - \tau_0)$. For $t \gg \tau_n$, g approaches $\Gamma\left(\frac{4}{3}\right)$.

The solid lines in Figure 2.3 are theoretical curves of the crystalline fraction and the density of grains versus normalized anneal time assuming a constant nucleation rate. The density of grains is normalized to the final density.

2.3.7 Crystallization from seed grains

Crystalline fraction is determined in Appendix C as a function of anneal time for crystallization from an initial seed density ρ_s assuming no nucleation:

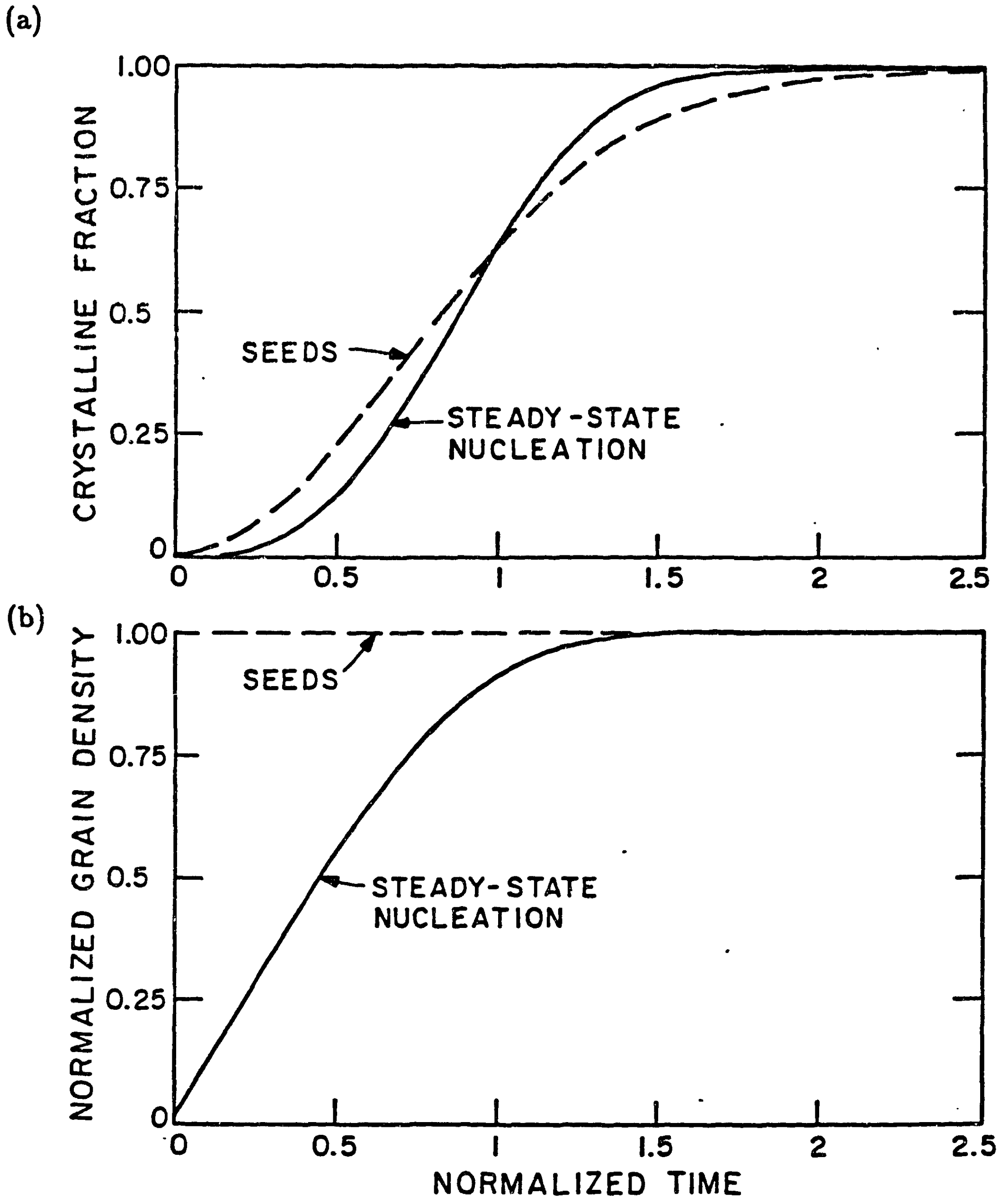

Figure 2.3: Theoretical plots of (a) crystalline fraction and (b) density of grains (normalized to final density) versus normalized time. The solid lines are for crystallization due to a constant nucleation rate. The dashed lines are for crystallization due to seed grains.

$$\chi_s = 1 - \exp\left[-(t/\tau_s)^2\right], \tag{2.22}$$

where τ_s is the characteristic time of crystallization in a seeded film:

$$\tau_s = 1/\sqrt{\pi v_g{}^2 \rho_s}. \tag{2.23}$$

The dashed lines in Figure 2.3 are theoretical curves of the crystalline fraction and the density of grains versus anneal time (normalized to τ_s) assuming crystallization from seed grains.

2.3.8 Competition between seeded and spontaneous crystallization

In implanted polycrystalline silicon films, seed grains which survive implantation may compete with grains that nucleate spontaneously. The crystalline areas resulting from these two sources may be considered independent, as is done in Appendices B and C The crystalline fraction as a function of time, then, is

$$\chi(t) = \begin{cases} 1 - \exp\left[t/\tau_s\right]^2 & t < \tau_0 \\ 1 - \exp\left\{-\left[(t - \tau_0)/\tau_n\right]^3 - \left[t/\tau_s\right]^2\right\} & t > \tau_0 \end{cases} \tag{2.24}$$

where τ_n and τ_s are defined in Eqns. (2.20) and (2.23) respectively.

The density of grains versus time is given by

$$\rho_g(t) = \rho_s + \int_{\tau_0}^{t} \epsilon r_n \left[1 - \chi(t')\right] \mathrm{d}t'. \tag{2.25}$$

Because of the complicated form of χ in Eqn. (2.24), this can only be solved numerically (by computer) or approximately (by a Taylor series expansion of the integrand, for example).

The final grain size is smaller than $1/\rho_s$ because any nucleation increases the density of grains. Also, the final grain size is larger than $1/[\rho_s + \rho_n(\infty)]$

since fewer grains nucleate than in an unseeded film because the amorphous fraction within which nucleation occurs is smaller. (ρ_n(t) is the density of grains assuming no initial seeds exist.)

2.4 Conclusions

The theory developed in this section predicts the crystallization behavior of implanted polycrystalline films and is embodied by Eqns. (2.24) and (2.25) and associated equations — crystalline fraction χ and density of grains ρ_g are the two quantities determined experimentally as functions of implant dose, anneal temperature, and anneal time and from which parameters of the crystallization model are extracted.

The dose dependence is found in the parameter ρ_s (in Eqn. (2.25)) as determined by Eqns. (2.1) through (2.5). The temperature dependence is found in the crystallization parameters τ_0, r_n, and v_g in Eqns. (2.11), (2.13) and (2.17). The time dependence is found in χ and ρ_g in Eqns. (2.24) and (2.25).

This theory predicts three plateaus in the plot of final grain size versus implant dose:

1. At *low doses*, the small degree of amorphization has little bearing on the morphology of the annealed film. Enough crystalline structure of each grain is retained to serve as a seed. The final grain size, therefore, should be approximately the same as before the implant and the texture should be unchanged.
2. At *intermediate doses*, a fraction of the grains are amorphized en-

tirely. Neighboring grains which survive the implant grow into the space formerly occupied by these grains. The resulting average grain size is therefore assumed to depend only on implant dose. Channeling effects should result in a "dose window", where most grains are amorphized and those that survive the implant do so because they are oriented with a major crystallographic direction parallel to the ion beam. Within this window, the final grain size should not be a strong function of implant dose and the annealed film should contain only grains that exhibit channeling effects.

3. At *large doses*, so few grains (oriented or otherwise) survive the implant that crystallization proceeds by the growth of homogeneously nucleated grains. Because nucleation and growth rates are strong functions of temperature, the grain size in this regime depends on anneal temperature but not on dose.

From this theory, orientation effects should be apparent in the second plateau only — the first plateau contains randomly-oriented grains from the as-deposited film and the third plateau contains nucleated grains.

The experimental results of this work support the theory as presented but requires a basic refinement: the microcrystals which survive implantation above 2×10^{15} ions/cm^2 are small enough that they must be regarded as sub-critical clusters. This results not in seeded crystallization, but in crystallization due to a large nucleation rate. (This does not necessarily preclude seed selection by ion channeling, since the clusters may retain the orientation of the as-deposited grain.)

The as-implanted cluster population is a strong function of implant dose and is also a function of cluster size. In Appendix A, an intermediate function ρ_A is defined as the distribution by size of the undamaged regions. This function includes the as-implanted cluster population. However, since ρ_A is not explicitly determined, a first-order model is proposed here. Consider a cluster with cross-sectional area A_C and thickness ϵ_c. For a single ion hit, assume that the probability of annihilation is proportional to ϵ_c since at large implant energies the distance between ion-nuclei interactions can be large. The "annihilation dose", then, is $Q' = CQ\epsilon_c$, where C is a constant. The survival probability is given by

$$\begin{aligned} P_C &= \exp\left(-Q'A_C\right) \\ &= \exp\left(-CQA_C\epsilon_c\right) \\ &= \exp\left(-C'Qn\right), \end{aligned} \tag{2.26}$$

where C' is a constant. A more exact formulation would consider that the clusters do not exist initially, but are a result of amorphizing most of a crystalline material. This could be represented by a dose offset, which would probably be a function of cluster size. The major point raised by Eqn. (2.26) is that the number of clusters of size n should decrease exponentially with implant dose and, furthermore, large clusters are amorphized faster than small clusters. From Eqns. (2.26) and (B.11), the final grain size increases exponentially with dose if the nucleation rate can be considered proportional to the number of clusters.

For the films used here, at doses below approximately 5×10^{15} ions/cm^2, the initial cluster population is so large that the film recrystallizes before a steady-state distribution is achieved. Above 5×10^{15} ions/cm^2, the initial cluster population is so small that no nucleation occurs during the transient time. Around 5×10^{15} ions/cm^2, few enough clusters exist that the nucleation rate is low during the transient period and the final grain size is actually larger than can be achieved at higher or lower doses.

Chapter 3

Experimental Method

This chapter describes how the polycrystalline silicon films are grown, implanted, annealed, and prepared for transmission electron microscopy (TEM). The last sections describe TEM and how the data is extracted from the micrographs.

3.1 Film Growth

Two-inch [100] lightly-doped *n* or *p*-type silicon wafers are cleaned using a standard RCA clean.

Immediately after the clean, the wafers are placed into a quartz-tube furnace to grow a thermal 1000Å SiO_2 film according to the following menu:

- 15 minutes at 1100°C in N_2;
- 46 minutes at 1100°C in O_2; and,
- 15 minutes at 1100°C in N_2.

One wafer is then set aside to check the oxide thickness.

The remainder are immediately transferred to an LPCVD system to deposit a layer of polycrystalline silicon. The deposition is accomplished by pyrolytic decomposition of silane (SiH_4) at approximately 640°C. The deposition rate is 135Å/minute.

Film thicknesses used here vary between 1000Å and 1600Å and are measured using a Nanospec thickness meter.

3.2 Implantation

All implants are carried out at room temperature using 100 KeV Si^+ ions at 0° incidence. The beam current is maintained at less than 10 μA to minimize wafer heating.

According to implant-range tables,[55] the projected range for these implants is 1469Å and the straggle (standard deviation) is 567Å.

The projected range and straggle for the damage profile are estimated from results published by Brice,[38] in which damage profiles are calculated for silicon implanted with phosphorus ions — since silicon and phosphorus have nearly the same atomic mass, the damage caused by silicon ions is assumed to be very similar. According to Brice, the peak damage for 100 KeV phosphorus ions is at approximately 60% of the projected ion range. The peak damage for silicon, then, is near 1000Å. Since the straggle of the damage profile of 100 KeV phosphorus ions is approximately 40% of the projected ion range, the straggle in silicon is about 600Å.

3.3 Recrystallization

The implanted films are diced into several pieces. Each piece is RCA cleaned prior to the anneal. The anneal is performed in a three-zone quartz-tube furnace in an N_2 ambient.

3.4 Preparation for Transmission Electron Microscopy

Each annealed sample is prepared for TEM by either lift-off or backside etching.

For lift-off, an sample is scribed and submerged in HF, an oxide etch which is very selective over silicon. After the HF etches the underlying oxide, it is carefully decanted, leaving most of the recrystallized film on the sample. De-ionized water is then poured on top of the sample. This action is usually violent enough to break off several pieces of film which float on the surface of the water. Some of these bits are then scooped up onto copper TEM specimen grids.

For backside etching, the back of a 2.5 mm square sample is first ground using a Gatan Dimple Grinder until it is an estimated 20–40 μm thick at the center. (The radius of curvature is 1 cm.) The sample is then placed face down in apiezon wax (black wax) and submerged in an anisotropic silicon etch: 3 parts CH_3COOH, 4 parts HNO_3, and 1 part HF. This etches through the silicon wafer to the oxide layer. When a membrane forms (after 5 to 10 minutes), the sample is dipped in HF to remove the oxide. The black wax is removed using trichlorethylene, acetone, and methanol.

3.5 Measurement Methods

3.5.1 Transmission Electron Microscopy

Transmission electron microscopy (TEM) operates by passing a a wide collimated beam of high-energy electrons (100–200 KeV, in this case) through a thin sample. Before hitting the sample, the beam is collimated and directed by a series of electromagnetic lenses. After passing through the sample, the beam is no longer collimated, but consists of a transmitted beam and several diffracted beams. These are focused and steered using additional electromagnetic lenses. Three types of micrographs are typical of TEM work: diffraction patterns, bright-field images, and dark-field images.

The diffraction pattern is obtained by focusing the transform plane of the sample onto a phosphorescent screen (for viewing) or onto a negative (for micrographs). The diffraction pattern yields qualitative information on the crystallinity and quantitative information concerning crystal orientations. Amorphous material produces diffuse rings. Small-grain polycrystalline material produces sharp rings which are actually the superposition of the diffraction patterns of the various grains. For large grained materials, individual spots in the rings can be observed.

The bright-field image is obtained by focusing the transmitted beam. The brightness of the resulting image is a function of the absorption and diffraction of the specimen. Amorphous silicon tends towards a uniform grey. Crystals will be light or dark, according to how much light is diffracted. The bright-field image is a good indicator of amorphous and crystalline regions. For the films used in these experiments, however, the bright-field image is not very good for resolving abutting grains.

The dark-field image is obtained by focusing some of the diffracted beam. A bright image is the result of a crystallite which diffracts in a particular direction. A black image is the result of a crystallite which does not diffract in that particular direction. Amorphous silicon diffracts small numbers of electrons and, so, appears dark, but not black. The dark-field image provides a fair method of estimating grain size even though grains are abutting.

To determine grain density and crystalline fraction, bright-field micrographs of the films are taken at a magnifications of 5,000–50,000×. Each micrograph covers an area of 275–2.75 μm^2, depending on the magnification. Between four and eight bright-field micrographs of each sample are usually taken to reduce statistical errors.

It is important to note that the crystalline fraction is *not* measured by TEM. Measurement from micrographs actually gives the "projected crystalline fraction". For example, a grain which is 100Å×100Å×100Å in a 1000Å film obscures an amorphous volume of 900Å×100Å×100Å. Zellama *et al.*[56] calculated crystalline fraction in silicon films from resistivity (sensitive to the true crystalline fraction) and therefore needed to allow a time for crystals to grow to span the thickness of the film. Because TEM measures the projected crystalline fraction, however, we do not need to worry about accounting for volumes less than the film thickness — the projected area of a grain will be $\pi {v_g}^2 t^2$ whether or not it is larger than the film thickness. Any grains that nucleate above or below a previously-nucleated grain serve the same function as the virtual grains utilized in Appendix B to calculate the crystalline fraction for a steady-state nucleation rate: these grains do not contribute to the projected crystalline fraction and they do not contribute to the measured density of grains.

Grain size in completely recrystallized film is determined from a dark-field micrograph taken at a magnification appropriate to the grain size: large enough magnification that the area can be measured, and small enough that many grains are included.

3.5.2 Density of Grains

The density of grains can only be determined for *partially* recrystallized films. In the films over approximately 30% recrystallized, several clumps contain an indeterminate number of grains — abutting grains in these films cannot be readily resolved. In films less than 30% recrystallized, there are few such clumps and the grains can be accurately counted. Each grain lying across boundary of a micrograph is counted as half. Similarly, any grain on the corner of a micrograph contributes only 0.25 towards the total grain count $n_{g,pic}$. When the total micrograph area is A_{pic}, the density of grains is

$$\rho_g = n_{g,pic}/A_{pic}. \tag{3.1}$$

From a statistical viewpoint, the number of grains appearing in a micrograph may be modeled as a Poisson process. The standard deviation of the number appearing, then, is $\sqrt{n_{g,pic}}$ and the standard deviation of the grain density is given by

$$\sigma_{\rho_g} = \rho_g/\sqrt{n_{g,pic}}. \tag{3.2}$$

3.5.3 Crystalline Fraction

Unlike grain density, the crystalline fraction can be measured on every micrograph. An image analyzer is used to total the crystalline or amorphous portions of each micrograph, whichever proves easier. The crystalline fraction is

$$\chi = A_{\chi,pic}/A_{pic} = 1 - A_{\alpha,pic}/A_{pic}, \tag{3.3}$$

where $A_{\chi,pic}$ is the total crystalline area and $A_{\alpha,pic}$ is the total amorphous area.

The statistical error of this measurement depends on whether $A_{\alpha,pic}$ or $A_{\chi,pic}$ is measured and on the distribution of sizes of the crystalline or amorphous regions. When the density of grains is also determined, the standard deviation of χ is taken to be

$$\sigma_\chi = 1.34(\chi/\sqrt{n_{g,pic}}). \tag{3.4}$$

The factor of 1.34 enters assuming a uniform size distribution (by radius) of the grains — this is the case for grains which nucleate at a steady-state rate. When the grains are all the same size, a factor of unity is be used instead.

When the crystalline area in a micrograph is not composed of discrete grains, the above statistics do not apply. In the absence of formulas describing the statistical size distribution of amorphous regions or of large crystalline regions, one of two methods is used to estimate the error:

1. When there is a large number of regions $n_{r,pic}$ which contribute to the measured area, the fractional error is taken to be $1/\sqrt{n_{r,pic}}$;

2. Otherwise, the fractional error is taken to be $\sigma/\sqrt{N_{pic}}$ where N_{pic} is the number of micrographs taken and σ is the standard deviation of the N_{pic} areas measured.

3.5.4 Grain Size

In the polycrystalline silicon films used here, grains in a TEM bright-field image cannot be resolved. The average area can only be determined by a dark-field image. In dark-field micrographs, only some grains can be readily resolved, partly because of contrast, and partly because of characteristic shape.

So few grains can be accurately measured that a nonstandard technique is used in which two grains are selected: one which appears larger than the average size, and one which appears smaller than the average size. The areas of these two grains are a loose bound to the average area. Because this is such a subjective method, the average area is only roughly determined: the two grain sizes differ by as much as a factor of five.

3.5.5 Experimental sources of error

In addition to statistical errors, the data may vary due to inconsistent processing parameters during deposition, implantation, or anneal: deposition temperature or time, ion dose or energy, or anneal temperature or time.

- *Deposition temperature.* The LPCVD system operates by the thermal decomposition of silane (SiH_4) gas diluted in N_2 as it flows over the wafers. Since the silane is more depleted for the last wafers than for the first, the system uses a temperature gradient so that the deposition rate is approximately the same for all wafers. The film morphology, therefore, may vary from wafer to wafer within one run.

- *Deposition time.* The shortest deposition time used is 7.5 minutes for a 1000Å film. The deviation is estimated to be 15 seconds, mostly due to irregularities in the start-up transient.
- *Ion dose.* The ion dose is expected to be consistent because it is monitored by the ion implanter by integrating the detected beam current; however, it may vary up to 10% across a wafer due an irregular scan of the ion beam.
- *Ion energy.* The ion energy may vary by 10 KeV, or 10%. This affects the depth distribution of the implant damage.
- *Anneal temperature.* Fluctuations in the temperature within the anneal tube have been observed, though these are usually less than 1°C. There have been occasions when the nitrogen supply had run out during an anneal. The effect this has on the anneal temperature is not known.
- *Anneal time.* The shortest anneal time used is 15 minutes. The deviation is estimated to be 5 seconds. The length of the rising temperature transient is not known, but is considered here to be insensitive to the anneal temperature. The thermocouple used to calibrate the temperature exhibits a transient time of about 5 minutes. The boat which is used to hold the samples may have a similar time constant.

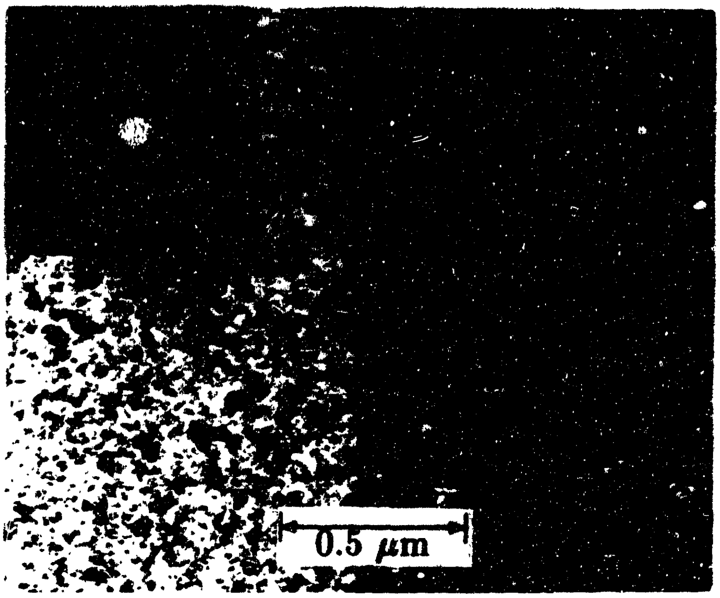

Figure 3.1: TEM micrograph of an as-deposited polycrystalline silicon film: the bright-field image is on the left, the dark-field image is on right, and the diffraction pattern is inset.

3.6 Morphology of the as-deposited film

Figure 3.1 is a micrograph of the as-deposited polycrystalline silicon. The grain size is 100–300Å. The texture of the films used here (thicknesses of 1000–1500Å) is not known. For 4400Å films deposited in the same system,[19] the grain size is larger and the texture is {110} within approximately 20° of normal incidence. The thinner films used in this thesis are probably not as uniformly oriented.

Chapter 4

Dose Dependence of Final Grain Size

This chapter investigates the dose dependence of final grain size and compares experimental results with the model developed in Chapter 2.

In 1981, Komem and Hall published a paper[15] on the effect of dose in polycrystalline films which were amorphized by implantation with germanium and recrystallized. Two implant doses were used (2×10^{15} ions/cm^2 and 4×10^{16} ions/cm^2) and two results were obtained: at the lower dose, the recrystallized film had a morphology similar to the original film; at the higher dose, the recrystallized film contained large (1 μm) dendritic grains, about 10 times larger than in the as-deposited film. By transmission electron microscopy (TEM), the as-implanted films were both 100% amorphous and the ability of the low-dose sample to recover its original morphology was attributed to to surviving grain boundaries.

The ability of the low-dose sample to recover its original morphology is attributed here to microcrystallites rather than to grain-boundary memory. The model is developed in Chapter 2. In this chapter, the final grain size

A_G is determined experimentally as a function of dose Q in self-implanted 1600Å LPCVD polycrystalline silicon films and the parameters of the model are fit to the curve of A_G versus Q.

4.1 Experiment and Results

1600Å polycrystalline films are implanted at doses ranging from 1×10^{14} to 5×10^{15} ions/cm^2 and annealed in N_2 at 700°C for 30 minutes. TEM samples of as-implanted and as-annealed films are prepared by lift-off. Diffraction patterns and bright and dark-field images are recorded. The final grain size is determined from the dark-field images by selecting two grains, one deemed larger and the other deemed smaller than the average. This gives a range within which the grain size is assumed to lie.

Micrographs of films implanted at 3×10^{14}, 5×10^{14}, 1×10^{15}, and 5×10^{15} ions/cm^2 are shown in Fig. 4.1 before and after anneal. Even at 1×10^{15} ions/cm^2, a few grains are visible in the dark-field image of the as-implanted film, though far fewer grains are visible than exist in the annealed film.

A plot of final grain size A_G versus implant dose Q is shown in Fig. 4.2. The bars indicate the range within which the final grain size is estimated to be.

The model developed in Chapter 2 uses several parameters, which are determined experimentally from a fit to the data shown in Fig. 4.2:

- A_G^{dep}, the initial grain size, is measured in an as-deposited film by TEM;
- A_D, the effective damage area, is fit to the transition region (of A_G

(a) As-implanted, 3×10^{14} ions/cm^2 As-annealed

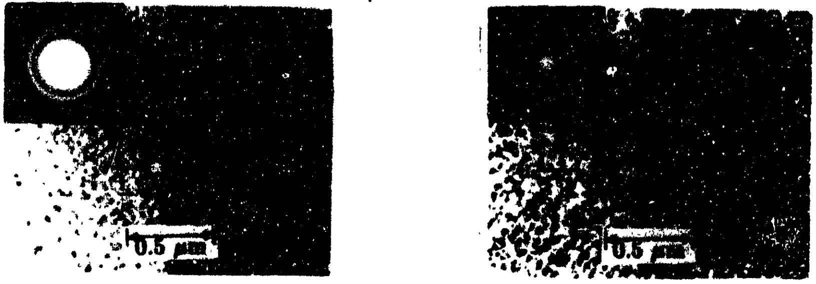

(b) As-implanted, 5×10^{14} ions/cm^2 As-annealed

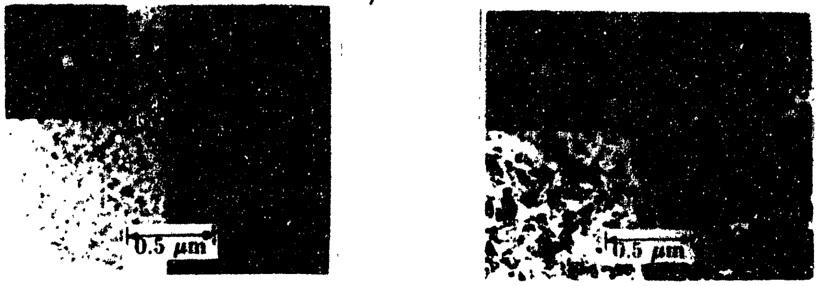

(c) As-implanted, 1×10^{15} ions/cm^2 As-annealed

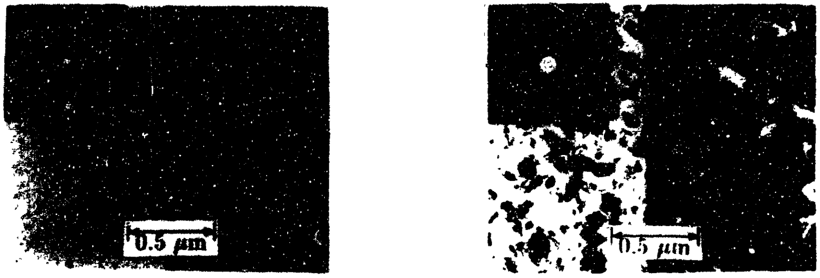

(d) As-implanted, 5×10^{15} ions/cm^2 As-annealed

Figure 4.1: Micrographs of as-implanted and as-annealed films for four implant doses: (a) 3×10^{14}, (b) 5×10^{14}, (c) 1×10^{15}, and (d) 5×10^{15} ions/cm^2. Diffraction patterns are inset. The left half of each micrograph is a bright-field image while the right half is a dark-field image.

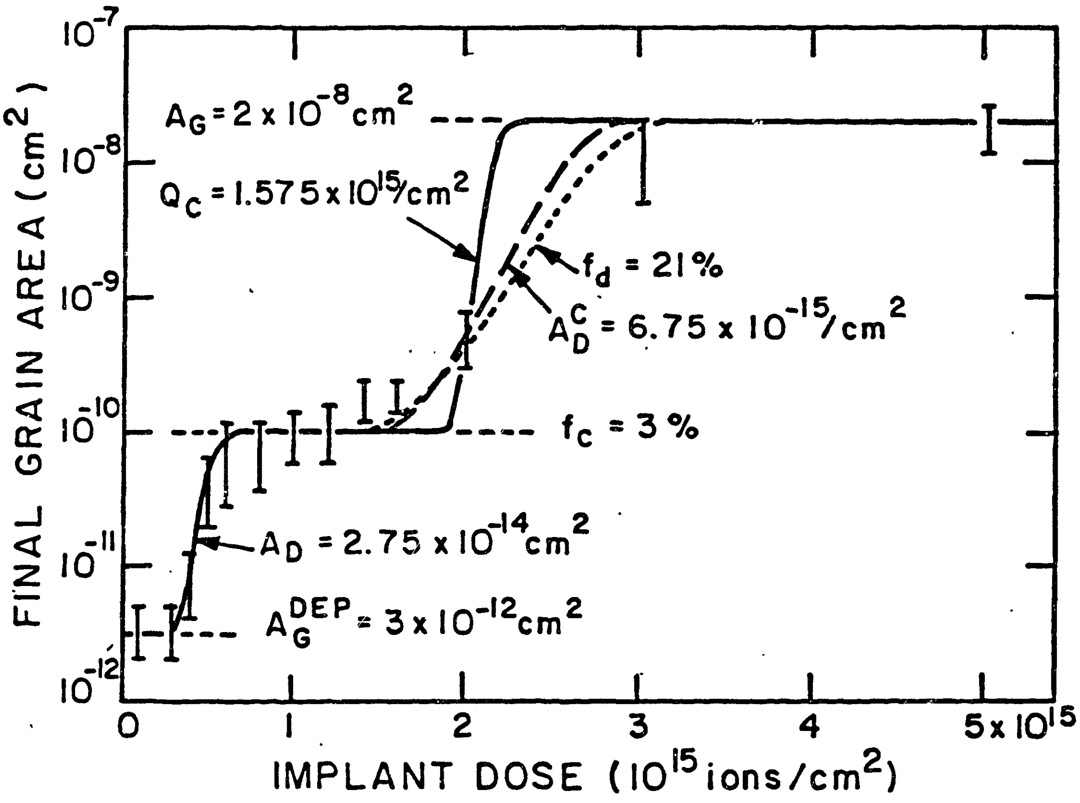

Figure 4.2: Final grain size of implanted and annealed polycrystalline silicon versus implant dose. The bars are the experimental bounds of the grain areas. Each parameter of the model is shown with the feature it corresponds to. The solid, dotted, and dashed lines represent the three models of ion-channeling effects described in the text.

versus Q) before the channeling plateau;

- f_c, the oriented fraction of the as-deposited grains, is determined by the height of the channeling plateau relative to the as-deposited grain size;
- One of three parameters to account for ion channeling is fit to the transition region after the channeling plateau (a channeling dose offset Q_C, a dechanneling fraction f_d, or an effective channeling damage area A_D^C); and
- $A_{G,n}$, the final grain size due to nucleation alone, is determined by the height the final plateau and is compared with the value calculated from the crystallization parameters (nucleation rate and growth velocity) using Eqn. (B.11).

The solid, dotted, and dashed lines in Fig. 4.2 correspond, respectively, to the "channeling-dose offset", "dechanneling fraction", and "effective channeling damage area" models of the channeling effect.

A paper by Zellama *et al.*[56] contains values for nucleation rate r_n and growth velocity v_g at temperatures of 560–600°C. Extrapolating this data to 700°C gives an estimate of r_n between 3×10^9 and $6\times10^{10}/\text{cm}^3\cdot\text{sec}$ and an estimate of v_g between 45 and 75 Å/sec. Using values of $1.3\times10^{10}/\text{cm}^3\cdot\text{sec}$ and 50 Å/sec, the final grain size from Eqn. (B.11) is 2 μm^2 (corresponding to a diameter of 1.6 μm) in agreement with the value of $A_{G,n}$ fit to the data in Fig. 4.2.

4.2 Discussion and Summary

The model developed in Chapter 2 for the dose dependence of the final grain size is supported by the experimental data presented here. This model calculates the percentage of grains which survive the implant using the statistics of the impact positions of the ions in conjunction with an effective damage area. A channeling plateau exists, as predicted, but it is not flat. The slope is assumed to be caused by different degrees of channeling in the various grains — each orientation could be characterized by a unique channeling parameter (Q_C, f_d, or A_D^C), but the resulting model becomes unwieldy and does not lend any additional insight into the physics involved.

The effective damage area used to model the damage is a very rough approximation to reality. Ion damage is a function of depth and might be represented better by a damage volume with a cross-sectional area dependent on depth, though analysis is probably intractable.

Three related experiments were performed by Kung *et al.*[19–21] to demonstrate seed selection by ion channeling (SSIC) using X-ray pole-figure analysis of the {110} texture in self-implanted polycrystalline films. Thick polycrystalline films (4400–4800Å) were required to overcome noise involved with the measurement. Also, unlike the films reported in this thesis, the implants were performed at 210 KeV and at low temperatures (≈80 K) in order to damage the entire thickness and maximize the channeling effect. (Channeling is enhanced at lower temperatures because of reduced thermal vibrations in the crystal lattice.)

- The first experiment[19] showed that a dose of 1×10^{15} ions/cm^2 and subsequent anneal produced films with a {110} texture confined to within 4° of the surface normal; whereas, the {110} texture of the as-deposited film was only within 20° of the surface normal.
- The second experiment[20] showed that texture of the film tracked with the implant angle when implanted at 0°, 1°, or 3° from normal incidence.
- The third experiment[21] correlated final grain size and the enhanced {110} texture with the implant dose.

From the data in the third experiment, the {110} texture can be correlated with the dose-dependence of the grain size, yielding an unexpected result: The annealed films exhibiting the highest degree of orientation correspond to a dose near the *bottom* of the "channeling plateau". From the model developed in Chapter 2, however, one would expect the highest degree of orientation to occur just below the nucleation plateau; that is, just before spontaneous nucleation affects the final grain size.

Since the films reported in this thesis are of a different thickness and implanted under different conditions, not all findings of this thesis necessarily apply to Kung's films. Lacking other evidence, however, it is assumed the thin films used here have a dose-dependent texture similar to Kung's.

Chapter 5

Temperature Dependence of Crystallization Parameters in Amorphized Silicon Films

This chapter describes an experiment to study the temperature dependence of nucleation and growth in a polycrystalline silicon layer amorphized by self-implantation. TEM measurements provide three basic crystallization parameters: transient time τ_0 (time before the onset of nucleation), steady-state nucleation rate r_n (per volume), and characteristic time of crystallization τ_n (measured from time τ_0). The nucleation rate and growth velocity are assumed to be time-independent (after time τ_0). The temperature dependence of the crystallization parameters is related to thermodynamic parameters in the classical theory of nucleation and growth.

From results presented in Chapter 4 (Fig. 4.2), the implant dose used here (5×10^{15} ions/cm^2) is large enough that crystallization by surviving grains can be neglected. Amorphized films are annealed at various temperatures and times. The crystalline fraction and number of grains are determined for each anneal condition and the data is fit by a classical model of nucleation and grain growth to give three crystallization parameters (τ_0, r_n, and τ_n) at each temperature. Growth velocity is calculated using Eqn. (2.20). The final grain size is extrapolated using Eqn. (B.11).

The parameters are compared to values reported the literature for the crystallization of silicon films deposited in the amorphous state. The major references are Zellama *et al.*,[56] Koster,[57] and Blum and Feldman.[58] Epitaxial <111> regrowth rate data, which is also referenced, was reported by Csepregi *et al.*[59]

Thermodynamic parameters within the classical theory of nucleation and growth are found using the temperature dependence of τ_0, r_n, and v_g in conjunction with Eqns. (2.12), (2.15) and (2.18).

5.1 Experiment and Results

Several 1000Å polycrystalline films are implanted at 5×10^{15} ions/cm^2. Pieces are partially annealed at temperatures of 580°C, 590°C, 600°C, 630°C, and 640°C. The anneal time at each temperature is varied over a time scale which is a function of anneal temperature. (The 580°C anneal times range from 50 to 100 hours, while the 640°C anneal times range from 2.5 to 4 hours.) TEM samples of the films are prepared by lift-off. Crystalline fraction and grain density for each anneal time are measured from several bright-field micrographs at a magnifications of 5,000–10,000×.

5.1.1 Density of grains and crystalline fraction

The density of grains and the crystalline fraction are measured from TEM micrographs. The micrographs in Figure 5.1, for example, show films annealed at 630°C for 4, 5.25, and 7.1 hours, respectively.

The grain density ρ_g is measured for films which are less than half recrystallized. In films over half recrystallized, there are several clusters of grains in which the grains can not be accurately counted. The data points in Fig. 5.2 show the density of nucleated grains as a function of anneal time and temperature.

The data points in Fig. 5.3 indicate the crystalline fraction χ as a function of anneal time and temperature, as calculated using an image analyzer.

5.1.2 Basic crystallization parameters

The model used to extract parameters is based on Eqns. (2.19) and (2.21) which use the premise that no nucleation or growth occurs during a transient time τ_0. Thereafter, the nucleation rate r_n and growth velocity v_g are assumed to be time-independent. Transient time and nucleation rate could be derived from the density of grains versus anneal time for a series of isothermal anneals; while, transient time and crystallization time could be derived from the crystalline fraction versus anneal time for a series of isothermal anneals. Since this method yields two values for transient time, these three parameters are derived instead by a single weighted least-squares fit of the data to Eqns. (2.19) and (2.21).

(a) 5×10^{15} ions/cm^2, 4 hours at 630°C

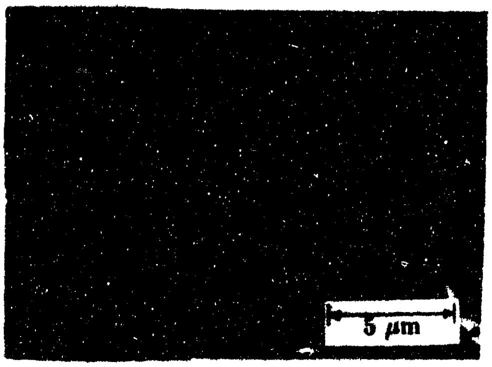

(b) 5×10^{15} ions/cm^2, 5.25 hours at 630°C

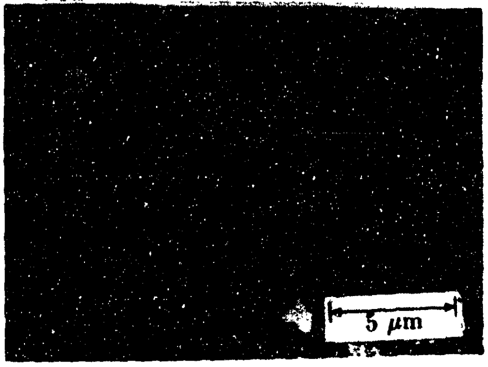

(c) 5×10^{15} ions/cm^2, 7.1 hours at 630°C

Figure 5.1: Bright-field micrographs of films implanted at 5×10^{15} ions/cm^2 and annealed at 630°C for three anneal times: (a) 4 hours, (b) 5.25 hours, and (c) 7.1 hours. Diffraction patterns are inset.

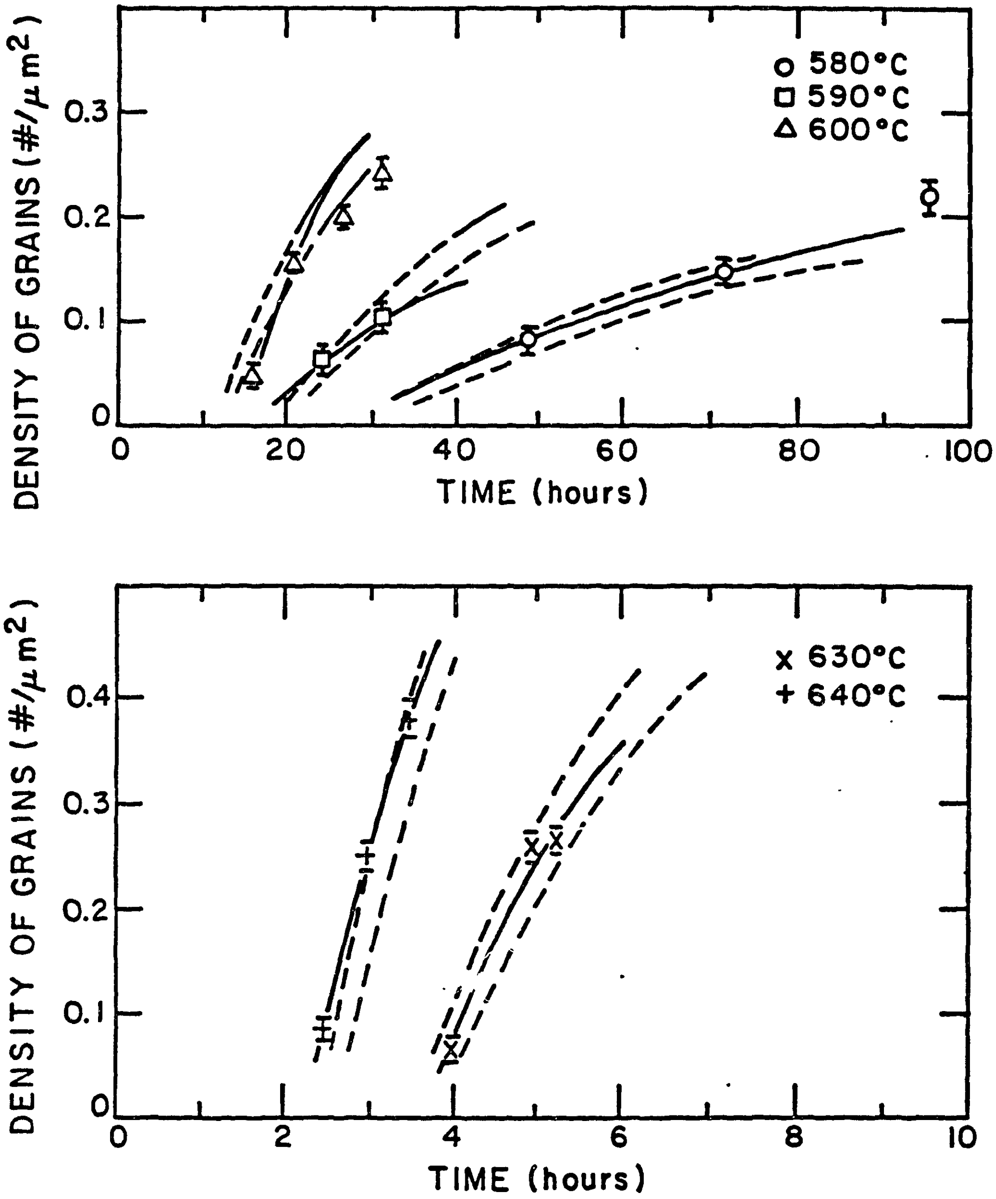

Figure 5.2: Density of grains versus anneal time at several temperatures in polycrystalline silicon implanted at 5×10^{15} ions/cm^2. Each solid line is fit to the data from a set of isothermal anneals by minimizing Eqn. (5.1). The dashed lines are calculated at ±1°C from the anneal temperatures using an Arrhenius model for growth and nucleation parameters.

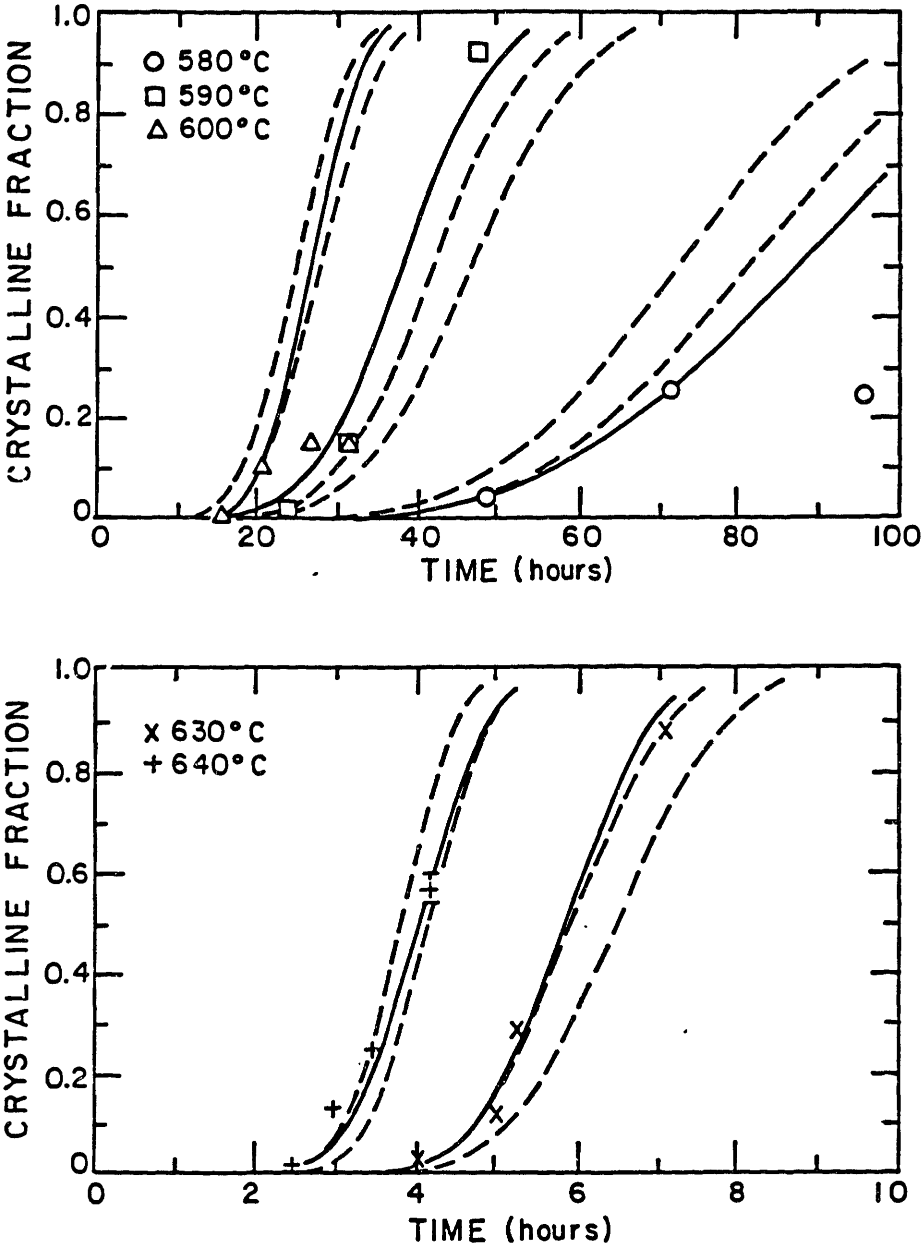

Figure 5.3: Crystalline fraction versus anneal time at several temperatures in polycrystalline silicon implanted at 5×10^{15} ions/cm^2. Each solid line is fit to the data from a set of isothermal anneals by minimizing Eqn. (5.1). The dashed lines are calculated at ±1°C from the anneal temperatures using an Arrhenius model for growth and nucleation parameters.

The following error criterion E is minimized with respect to τ_0, ϵr_n, and τ_n:

$$\begin{aligned} E(\tau_0, \epsilon r_n, \tau_n) &= W \sum_{i=1}^{n_G} \left[\epsilon r_n \tau_n g(u_i) - \rho_{g,i}\right]^2 \\ &+ \sum_{i=1}^{n_\chi} \left[1 - \exp(-u_i^3) - \chi_i\right]^2 , \end{aligned} \tag{5.1}$$

where n_G is the number of grain-density data points collected and n_χ is the number of crystalline-fraction data points collected. The weight W normalizes the grain-density data to the highest measured density of grains so that both sums are of the same order of magnitude. The transient time and crystallization time enter the equation in the normalized-time parameter $u_i = (t_i - \tau_0)/\tau_n$. The function $g(u)$ is defined is Eqn. (B.9).

The solid lines in Figs. 5.2 and 5.3 are the results of fitting τ_0, ϵr_n, and τ_n to the data for each temperature. However, three of the data points, though shown, are not used in the fit: the 96 hour anneal at 580°C, and the 27 and 31 hour anneals at 600°C. The reason these three data points deviate so far from theory is subject to conjecture. Some possibilities are: the growth rate may decrease due to impurity segregation; the different wafers received slightly different implant doses, which could affect any of the parameters; or, some of the samples may have become contaminated.

Figure 5.4 shows transient time as a function of temperature. The activation energy (solid line) is 2.7 eV. The literature contains no previous report of transient time values in silicon, although Koster[57] did show that the nucleation rate was time-dependent in freestanding amorphous silicon films prepared by electron beam evaporation at room temperature.

From Eqn. (2.12) and using kT of 0.075 eV, the experimental tempera-

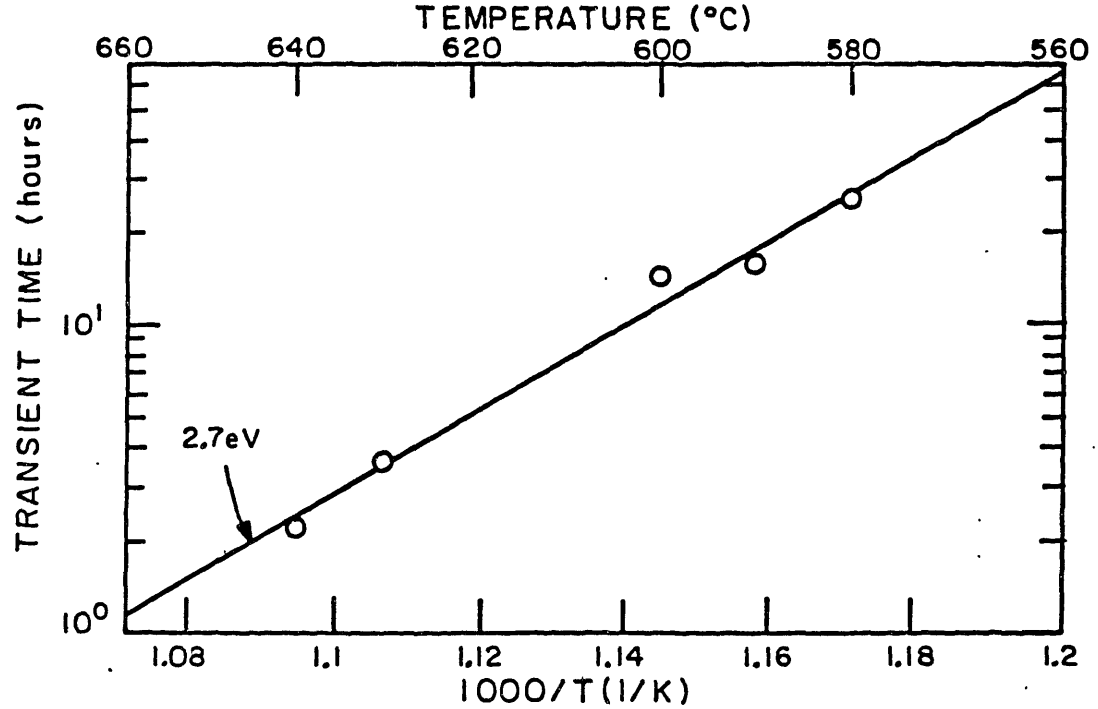

Figure 5.4: Transient time as a function of temperature in polycrystalline silicon films amorphized by self-implantation. The solid line is fit to the data and corresponds to an activation energy of 2.7 eV.

ture dependence of τ_0 indicates that the activation energy for self-diffusion in amorphous silicon, E_d, is 2.8 eV.

Figure 5.5 shows the nucleation rate as a function of temperature. The activation energy (solid line) is 5.1 eV. Also shown are values from papers by Zellama *et al.*[56] and by Koster.[57] Zellama measured growth nucleation rates in amorphous silicon films which were deposited at room temperature and at 570°C. Both of these papers cite an activation energy of 4.9 eV. For amorphous silicon films deposited at room temperature, however, Zellama found an activation energy of 9 eV. The high value could be in error if those films exhibited a transient time for crystallization.

From Eqn. (2.15) and the temperature dependence of τ_0 and r_n, the maximum free energy of formation of a cluster ΔG_n^* is 2.4 eV.

Figure 5.6 shows the characteristic crystallization time $\tau_n$as a function of temperature. The activation energy (solid line) is 3.9 eV. The data from the literature are from Zellama *et al.*,[56] Koster,[57] and Blum and Feldman.[58] Blum and Feldman measured optically a crystallization time in amorphous silicon films prepared by electron beam evaporation at 200°C–300°C and calculated an activation energy of 3.1 eV. This activation energy is not related to a particular crystallization process; but, rather, is the result of a number of processes, as can be seen in the definition of τ_n (Eqn. (2.20)).

The dashed lines in Figs. 5.2 and 5.3 illustrate the effect of varying the temperature by ±1°C. These lines are estimated by calculating (for each temperature) τ_0, ϵr_n, and τ_n, assuming the Arrhenius forms plotted in Figs. 5.4– 5.6. These lines indicate the error that could be introduced by a variation in anneal temperature of ±1°C.

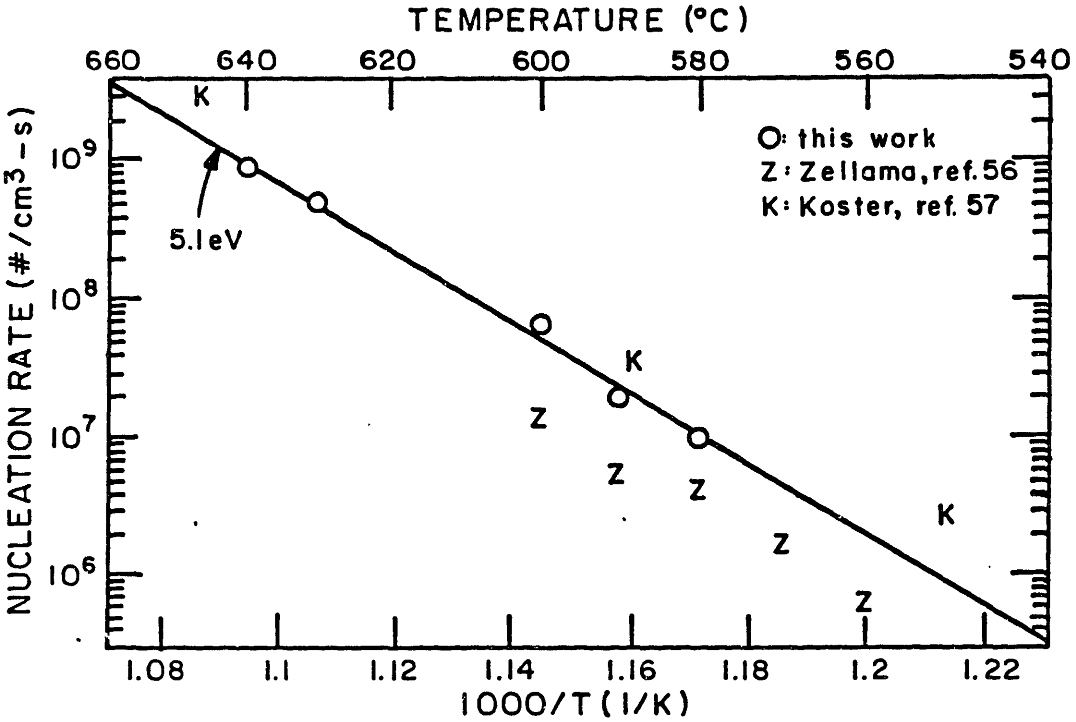

Figure 5.5: Nucleation rate as a function of temperature. The nucleation rate from this work is from polycrystalline silicon films amorphized by self-implantation. The data from the literature is from silicon films deposited in the amorphous state. The solid line is fit to the data from this work and corresponds to an activation energy of 5.1 eV.

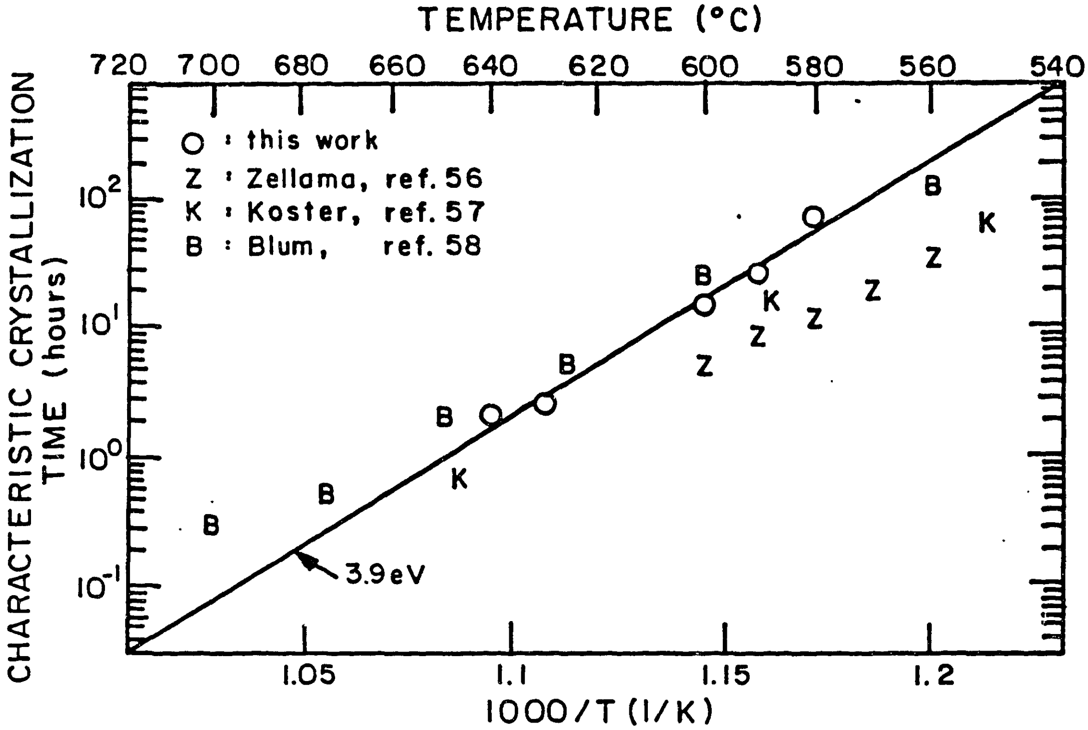

Figure 5.6: Crystallization time as a function of temperature. The characteristic crystallization time from this work is from polycrystalline silicon films amorphized by self-implantation. The data from the literature is from films deposited in the amorphous state. The solid line is fit to the data from this work and corresponds to an activation energy of 3.9 eV.

5.1.3 Growth velocity

Growth velocity v_g is calculated from ϵr_n and τ_n using a form of Eqn. (2.20):

$$v_g = \sqrt{\frac{3}{\pi \tau_n{}^3 \epsilon r_n}} \tag{5.2}$$

Figure 5.7 shows v_g as a function of temperature. The activation energy (solid line) is 3.3 eV. Also shown are data from several sources: Zellama *et al.*[56] (E_{v_g} of 2.4–4.9 eV); Koster[57] (E_{v_g} of 2.9 eV); and Csepregi *et al.*[59] (E_{v_g} of 2.35 eV). The data from Csepregi *et al.* is the slow <111> epitaxial regrowth velocity.

The growth velocity extracted here is lower than that reported in the literature and it is also has a larger activation energy than expected.

From Eqn. (2.18), E_d, and the temperature dependence of v_g, ΔG_{a-x} can be determined. The activation energies found here, however, yield a negative value (−1.0 eV/atom), which is not realistic. The activation energy of v_g must be less than E_d (2.8 eV) to be consistent with classical theory. The grains observed here exhibit twinning, which is typical in crystallized silicon films. Possibly, grain growth does not proceed by the same mechanisms used to describe growth of small clusters.

5.1.4 Final grain size

The final grain area A_G is calculated from Eqn. (B.11) using nucleation rate r_n and growth velocity v_g. Figure 5.8 shows the extrapolated final grain diameter, which is the diameter of a circle of area A_G. The graph shows that a slightly larger grain size can be achieved by crystallizing at lower temperatures.

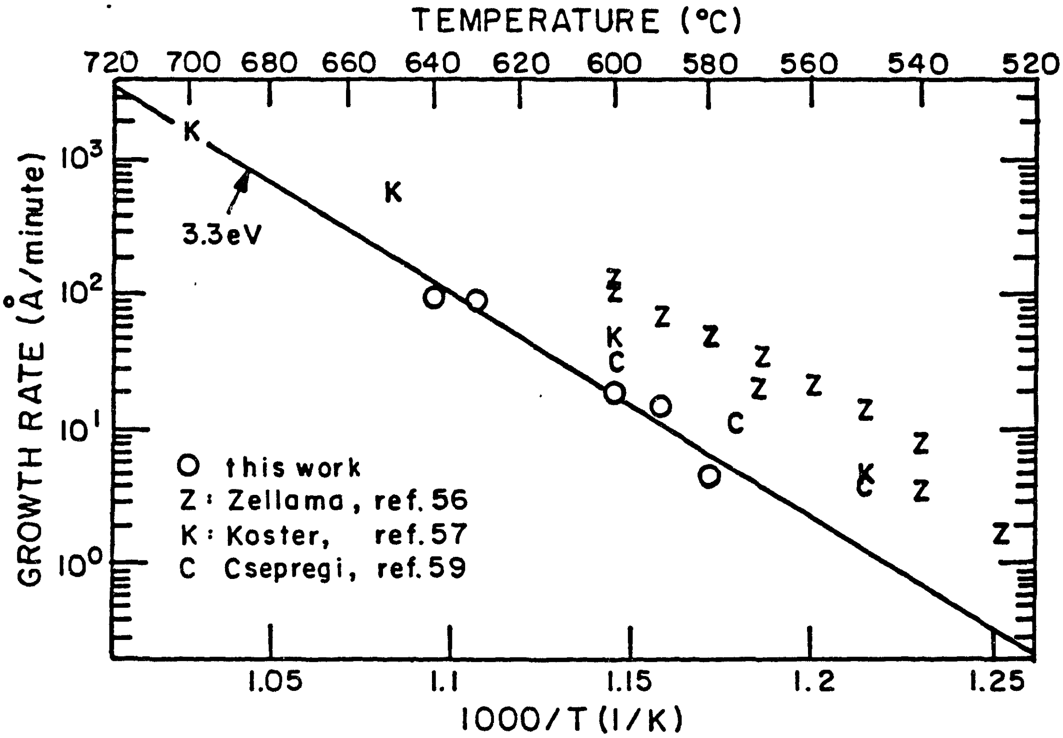

Figure 5.7: Growth velocity as a function of temperature in polycrystalline films amorphized by ion implantation. The growth velocity from this work is from polycrystalline silicon films amorphize by self-implantation. The data from Zellama and from Koster is from films deposited in the amorphous state. The data from Csepregi is the slow <111> epitaxial regrowth velocity. The solid line is fit to the data from this work and corresponds to an activation energy of 3.3 eV.

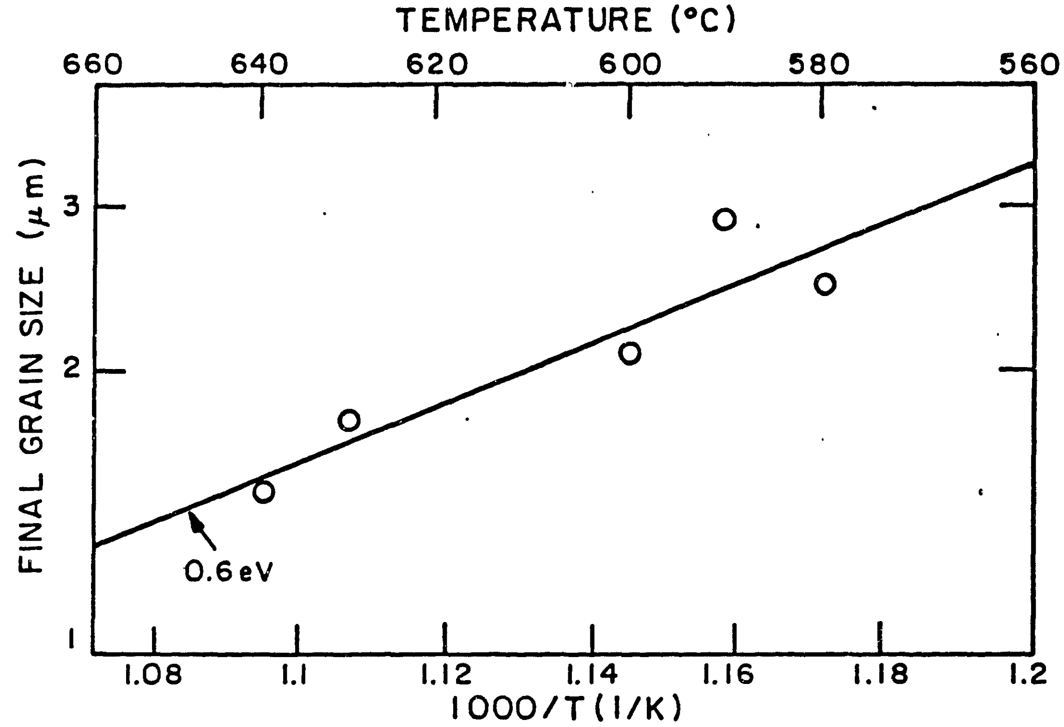

Figure 5.8: Grain size as a function of temperature, extrapolated from the growth and nucleation rates. The solid line is fit to the data and corresponds to an activation energy of 0.6 eV.

The grain size in completely recrystallized films is found from TEM dark-field images to be approximately 1–2 μm, in agreement with the values extrapolated from partially crystallized samples.

5.2 Summary and Discussion

Crystallization parameters are found as a function of temperature for a polycrystalline silicon film amorphized by self-implantation. The spontaneous nucleation rate r_n and recrystallization time τ_n are consistent with values found in the literature, even though the films in those experiments were deposited in the amorphous state.

A significant transient time τ_0 is found in the implanted films. This has not been reported before for silicon, although Koster[57] did show a time-dependent nucleation rate in an amorphous silicon film deposited at room temperature, but did not give a value for the transient time. The presence of a transient time might explain the anomalous activation energy measured for nucleation rate in room-temperature deposited films in the paper by Zellama *et al.*[56]

Implanting polycrystalline films at a high dose probably ensures that no crystalline clusters exist. During the transient time, the cluster population approaches a quasi-equilibrium distribution which leads to a steady-state nucleation rate. Films deposited in the amorphous state at elevated temperatures could have a significant cluster population, resulting in a negligible transient time. In films deposited at room temperature, the cluster population could be small enough to result in an observable transient time.

Other researchers have observed two optical states of amorphized silicon[60–62]: the defect-saturated (as-implanted) state, and the thermally-stabilized (annealed) state. The defect-saturated state is characterized by a refractive index 12% larger than in crystalline silicon. After two hours at 500°C, the refractive index drops to only 8% larger than in crystalline silicon and is then stable until crystallization. The refractive index was found to correlate with the dangling-bond density. Since the defect-saturated state lasts for only two hours at 500°C (and presumably less time at higher temperatures) the transient time observed here appears to be related neither to these optical states nor to the high density of dangling bonds in the as-implanted films.

The solid-phase crystal growth velocity v_g and final grain size A_G are inferred from ϵr_n and τ_n. Because the growth velocity is lower than expected, it may be a function of anneal time or grain size, in which case the Avrami equation is no longer valid. The low growth velocity could be due to contamination. The activation energy of v_g is higher than expected — in fact it leads to the erroneous conclusion that the crystalline phase is unstable. The activation energy of the growth velocity is found by assuming that the mechanism responsible for cluster growth (phase transitions of individual atoms at the amorphous-crystalline interface) is also responsible for crystal growth.

It is probably not possible to use anneal cycles to exploit the transient time in order to obtain a much larger grain size than has been achieved to date. To exploit the transient time, the film needs to be annealed just long enough to produce a few seeds. Then the film must then be cooled in such a manner that the population of clusters decreases. Films which were deposited at elevated temperatures exhibited no transient time, even though they were probably stored at room temperature. This indicates that cooling a partially annealed sample will probably freeze the cluster distribution.

The transient time can probably be utilized in epitaxial lateral overgrowth. The overgrowth distance should be proportional to $\tau_0 + \tau_n$.

The growth rate in silicon can be greatly enhanced by implantation during an anneal[63] (hot implantation). It may be possible to exploit the effect of implantation to achieve large grains. In material with a few nucleated grains, a hot implant may inhibit the nucleation rate while enhancing the growth rate of existing grains.

This experiment demonstrates that the crystallization behavior of polycrystalline silicon films amorphized by self-implantation is similar to the crystallization behavior of silicon films deposited in the amorphous films. It is found, however, that nucleation and growth in amorphized films proceed only after a transient time, which is a function of anneal temperature. This has been observed before only in amorphous films deposited at room temperature. From the temperature variation of crystallization, two thermodynamic parameters of the classical model of nucleation are calculated: the maximum free energy of formation of a crystal cluster is 2.4 eV; and the energy of self-diffusion in amorphous silicon is 2.8 eV. The grain size in completely recrystallized films is found by dark-field TEM to be 1–2 μm. This is in agreement with the calculated final grain size, as extrapolated from the nucleation and growth rates of partially crystallized films.

Chapter 6

Crystallization in a "Seeded" Amorphous Film

In Chapter 4, the three plateaus in the plot of final grain size as a function of implant dose are explained in terms of an effective damage area A_D associated with every ion. Below a dose of 3×10^{14} ions/cm^2 few grains are completely amorphized, though the level of amorphization is large enough that few crystalline areas are apparent from transmission-electron diffraction images. Above a dose of approximately 3×10^{15} ions/cm^2 crystallization appears due to nucleation by random cluster formation. At intermediate doses (6×10^{14}–2.5×10^{15} ions/cm^2), the final grain size is a relatively weak function of implant dose. In the model of Chapter 2, this plateau was predicted and attributed to ion channeling — over this range, some grains are assumed to survive because the ion channeling that occurs in specifically-oriented grains results in less damage than that produced in a randomly-oriented grain.

In a related experiment published by Kung and Reif,[21] three plateaus were again observed, but the <110> texture was found to be strongest at the *lower* end of the channeling plateau. If this plateau were indeed due to ion channeling, the <110> texture would have been stronger at the highest dose of the channeling plateau.

The experiment presented here examines the crystallization behavior of polycrystalline silicon implanted at 2×10^{15} ions/cm^2 (at the upper end of the channeling plateau) to determine whether the grains in the annealed film grow from seed grains (grains which survived the implant), as assumed in the model of implant damage in polycrystalline films. This is a more direct method of assessing the as-implanted state than by measuring the grain size *after* 100% crystallization.

6.1 Experiment and Results

A 1500Å polycrystalline film is implanted at 2×10^{15} ions/cm^2 and diced into several pieces which are then annealed at 580°C in N_2 for durations of 15 minutes to 3 hours. Where possible, TEM samples of the films are prepared by lift-off. For anneal times less than one hour, here, the films do not lift off the substrate and TEM samples are prepared by backside etching, instead. Grain density ρ_g and crystalline fraction χ are measured from several bright-field micrographs at a magnification of 50,000×.

Figure 6.1 shows bright-field micrographs and diffraction patterns of films annealed at 0.5, 1.5, and 2.5 hours.

A plot of the density of grains ρ_g as a function of anneal time is shown in Fig. 6.2. The density of grains is measured for anneal times up to one hour. (At longer anneal times, individual grains cannot always be resolved.) The

(a) 2×10^{15} ions/cm^2, 0.5 hours at 580°C

(b) 2×10^{15} ions/cm^2, 1.5 hours at 580°C

(c) 2×10^{15} ions/cm^2, 2.5 hours at 580°C

Figure 6.1: Bright-field Micrographs of films implanted at 2×10^{15} ions/cm^2 and annealed at 580°C for four anneal times: (a) 0.5 hours, (b) 1.5 hours, and (c) 2.5 hours. Diffraction patterns are inset.

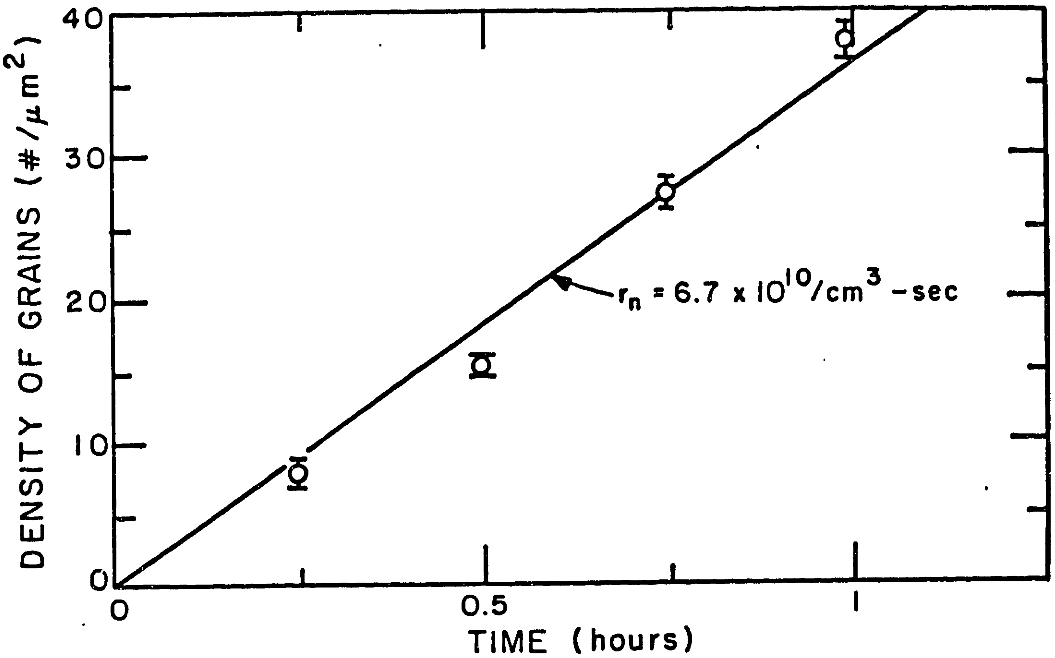

Figure 6.2: Density of grains as a function of anneal time at 630°C for polycrystalline silicon implanted at 2×10^{15} ions/cm^2. The solid line corresponds to theory (Eqn. (2.21)) assuming crystallization is due to a steady-state nucleation rate of 6.7×10^{10}/cm^3·sec.

solid line corresponds to theory (Eqn. (2.21)) assuming crystallization is due to a steady-state nucleation rate of 6.7×10^{10}/cm^3·sec.

If crystallization were from seeds, the density of grains would be constant; so, this indicates that crystallization is from nucleated grains. At 580°C, the nucleation rate in amorphous silicon[56,57] is about 1×10^7/cm^3·sec and is approximately the same as the nucleation rate in amorphized polycrystalline silicon (Chapter 5), nearly four orders of magnitude smaller than the steady-state nucleation found here. This large nucleation rate could be attributed to a large number of microcrystalline clusters in the as-implanted

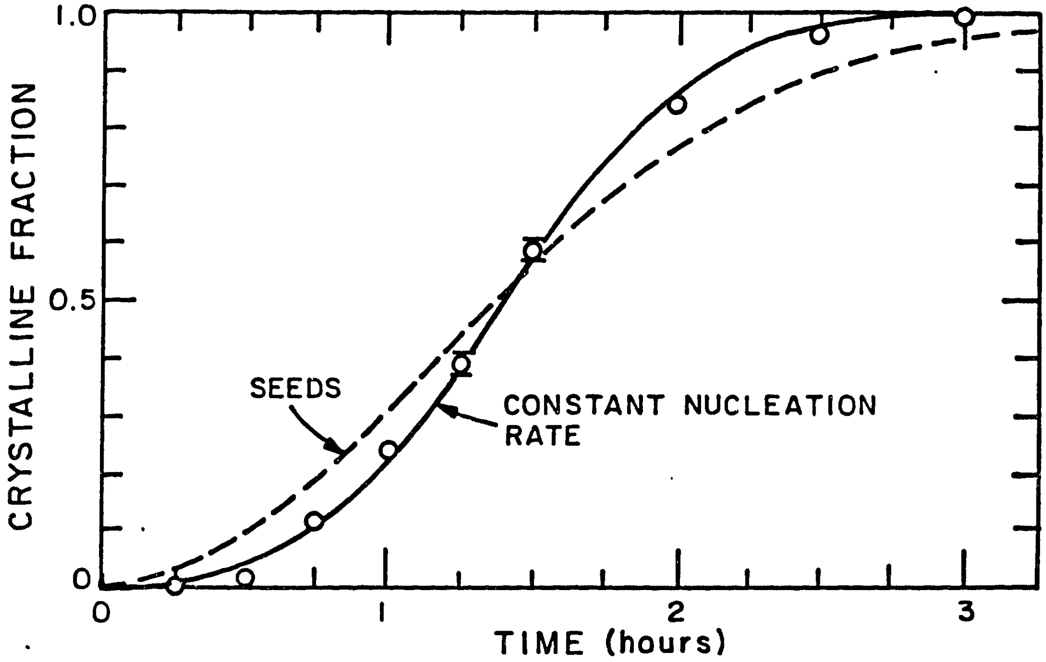

Figure 6.3: Crystalline fraction as a function of anneal time at 630°C for polycrystalline silicon implanted at 2×10^{15} ions/cm^2. The dashed line is the best fit of theory assuming seeded growth (Eqn. (2.22)). The solid line is the best fit of theory assuming nucleated growth (Eqn. (2.19)).

film, which would enhance the nucleation rate.

The crystalline fraction χ is calculated using an image analyzer and is shown in Fig. 6.3. The solid line is the theoretical crystalline fraction assuming spontaneous crystallization (Eqn. (2.19)) for a characteristic crystallization time τ_n of 1.58 hours. The dashed line is the best fit of Eqn. (2.22), which corresponds to seeded crystallization. This indicates again that crystallization is due to nucleated crystallites.

Using the above values of nucleation rate and characteristic crystallization time, the growth rate v_g from Eqn. (2.20) is 14 Å/minute, approximately the same as the slow <111> epitaxial growth rate.[59] Note that v_g is an average growth rate. The growth rate is also estimated from direct measurements of the largest grains. Since the grains are elliptical, there is a fast and a slow growth rate. Direct measurements indicate that the growth rate is 25 Å/minute along the major axis and 9 Å/minute along the minor axis. The effective radial growth rate (as used in Eqn. (2.20)) is the geometric mean of these. As determined by direct measurement of the largest grains, the effective radial growth rate is 15 Å/minute, in good agreement with the value found using the Avrami-Johnson-Mehl formulation.

From the values for r_n and v_g, the final grain size is extrapolated to be 0.15 μm using Eqn. (B.11). This is comparable to the value estimated from the dose-dependent study of grain size (Fig. 4.2) which is approximately 0.25 μm.

A cross-sectional TEM (XTEM) sample has been prepared from the film annealed for 0.75 hours. The micrographs in Fig. 6.4 show the single-crystal silicon substrate (bottom layer) with a 1000Å oxide above it. The next layer is the 1500Å film which has been implanted and partly recrystallized. Note that the grains are at the top surface, indicating that nucleation is occurring at or near the top surface. Therefore, nucleation can be treated as a *surface* nucleation rate, and the results of Chapter 4 (A_G vs. Q) apply for thinner films as well. (The films in Chapter 4 are 1600Å thick.)

(a) XTEM at 60,000×

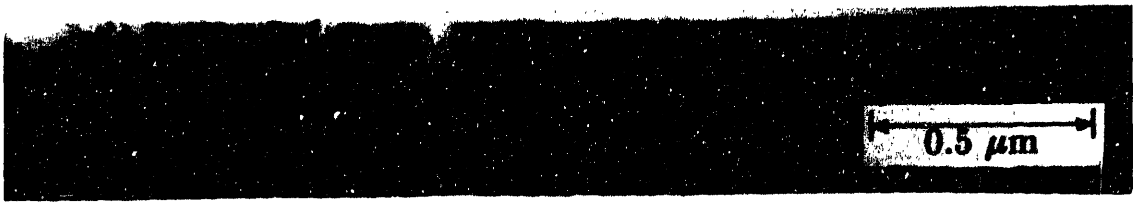

(b) XTEM at 200,000×

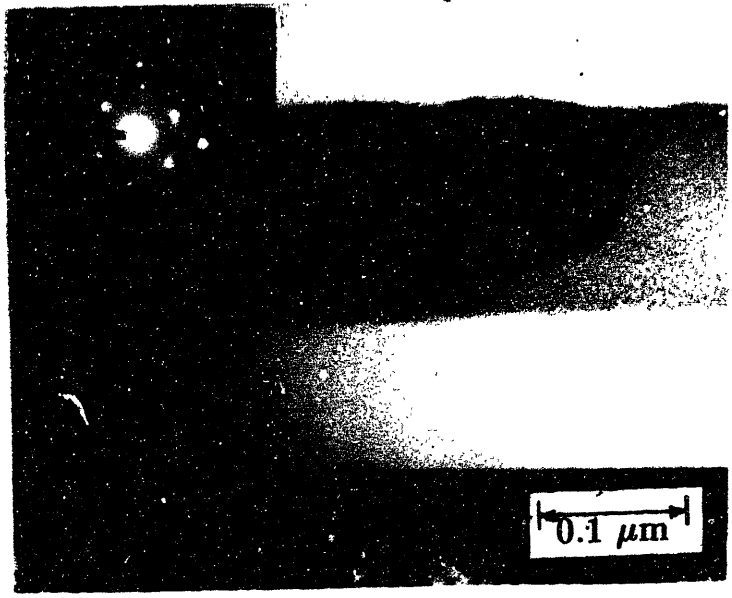

Figure 6.4: Cross-sectional TEM bright-field micrographs of a film implanted at 2×10^{15} ions/cm^2 and annealed at 580°C for 0.75 hours, at magnifications of (a) 60,000×, and (b) 200,000×. From the bottom up, the layers are: the single-crystal silicon substrate; a 1000Å oxide; and a 1500Å partially recrystallized film with grains at the top surface.

6.2 Summary and Discussion

The experimental results presented here demonstrate that for a polycrystalline silicon film implanted at 2×10^{15} ions/cm^2, crystallization is from nucleated crystallites, and not from seeds which survived the implant. The nucleation rate for this film is considerably larger than in amorphous silicon or in polycrystalline silicon amorphized at a larger dose. This could be because implantation leaves microscopic regions (clusters) which are not fully amorphized. Such regions would enhance the nucleation rate.

In Chapter 2, to determine the dose-dependence of final grain size we had assumed that a grain either survives the implant or is amorphized completely. The results presented here, however, indicate that a range of states may exist — an amorphized grain can exhibit a large nucleation rate (due to microcrystals), which apparently decreases with increasing implant dose. To first order, the number of these clusters should drop exponentially with implant dose, accompanied by an exponential drop of the "implantation-induced" nucleation rate.

The equations governing the crystallization behavior include a surface nucleation rate ϵr_n, from which r_n has been calculated. Because implantation-induced nucleation here is a surface phenomenon, the value of r_n will vary with the film thickness and only ϵr_n should be used. Similarly, spontaneous nucleation has been generally considered to be a surface phenomenon and perhaps should be treated as such. However, as in the literature, the practice of stating bulk nucleation rates is continued in this thesis.

Chapter 7

Dose Dependence of Crystallization Parameters in Amorphized Silicon Films

The nucleation rate in amorphized polycrystalline silicon films (5×10^{15} ions/cm^2), determined in Chapter 5, is near the nucleation rate in silicon films deposited in the amorphous state.[56,57] Also, the characteristic crystallization time determined in Chapter 5 is comparable to the crystallization time in films deposited in the amorphous state.[56,57,58] Transient nucleation, however, has not been reported except by Koster[57] for amorphous silicon films deposited *at room temperature.* It is suggested in Chapter 5 that this is because there are few clusters in silicon films deposited at sufficiently low temperature and in films amorphized at sufficiently high doses. The films of Chapter 5 are considered here to be "100% amorphous", more amorphous than deposited amorphous silicon, which has an as-deposited cluster population.

The experiment presented in this chapter investigates the dose dependence of the measured crystallization parameters (τ_n, r_n, τ_0) and derived parameters (v_g, A_G) near the "complete amorphization" dose of 5×10^{15} ions/cm^2.

7.1 Experiment and Results

Three 1500Å polycrystalline films are implanted at 4×10^{15}, 5×10^{15} and 5×10^{15} ions/cm^2. Small pieces are partially annealed at 630°C for anneal times ranging from 0.25 to 5 hours. TEM samples are prepared by backside etching. The crystalline fraction and grain density for each dose and anneal time are determined from several bright-field micrographs at magnifications of 5,000–10,000×. The crystallization parameters are then extracted for each dose.

7.1.1 Density of grains and crystalline fraction

The density of grains and the crystalline fraction are measured from bright-field TEM micrographs, such as shown in Fig. 7.1. The density of grains $\rho_g(t)$ is indicated in Fig. 7.2 and the crystalline fraction $\chi(t)$ is indicated in Fig. 7.3. The solid lines are fit to theory by minimizing Eqn. (5.1). The 1, 1.5, and 2 hour data points from the 5×10^{15} ions/cm^2 implant are from a different area of the wafer than the other points and, though self-consistent, do not fit well with the remaining results. In the rest of this chapter, these are called the "$5^-\times10^{15}$ ions/cm^2" results and the other data points are called the "$5^+\times10^{15}$ ions/cm^2" results because the different crystallization parameters can be attributed to the variation of implant dose across the wafer.

These plots indicate that crystallization takes longeı as the dose increases, even though the characteristic crystallization time is longer at 5×10^{15} ions/cm^2 than at the higher dose. Only at the higher dose is a transient nucleation time observed.

7.1.2 Crystallization parameters

The source of the dose-dependence of the crystallization time is rooted in the nucleation rate. All growth velocities here are within 10% of the growth velocity found in Chapter 5 for a 1000Å film implanted at 5×10^{15} ions/cm^2 and annealed at 630°C. The nucleation rate, however, is sensitive to the cluster population and, therefore, is sensitive to the implant dose. Figure 7.4 shows the normalized nucleation rate as a function of implant dose. Also included is a "2×10^{15} ions/cm^2" data point (ϵ=1500Å) from Chapter 6. The normalized nucleation rate is calculated using Eqn. (2.20):

$$r_n/r_n' = (\tau_n/\tau_n')^{-3} \tag{7.1}$$

where r_n' and τ_n' are values from Chapter 5 for 100% amorphous silicon. This form is used for the following reasons:

- The crystalline fraction is measured over a large range of anneal times; whereas, the grain density is only measured for $\chi(t) < 30\%$. The crystallization time, therefore, may be considered more reliable.
- The "$5^+\times10^{15}$ ions/cm^2" data includes no grain density information.

Equation (7.1) assumes that v_g and ϵ which determine τ_n are the same as v_g' and ϵ' which determine τ_n'. Since implantation-induced nucleation occurs

(a) 4×10^{15} ions/cm^2, 1 hour at 630°C

(b) 4×10^{15} ions/cm^2, 1.5 hours at 630°C

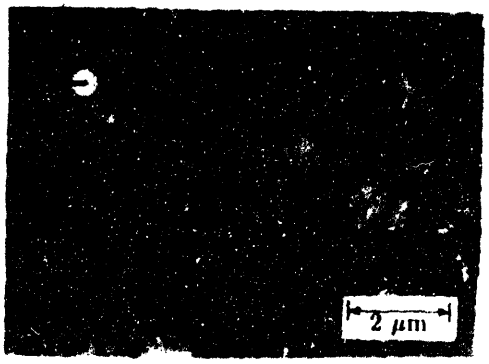

(c) 4×10^{15} ions/cm^2, 2.5 hours at 630°C

Figure 7.1: Bright-field micrographs of films implanted at 4×10^{15} ions/cm^2 and annealed at 630°C for three anneal times: (a) 1 hour, (b) 1.5 hours, and (c) 2.5 hours. Diffraction patterns are inset.

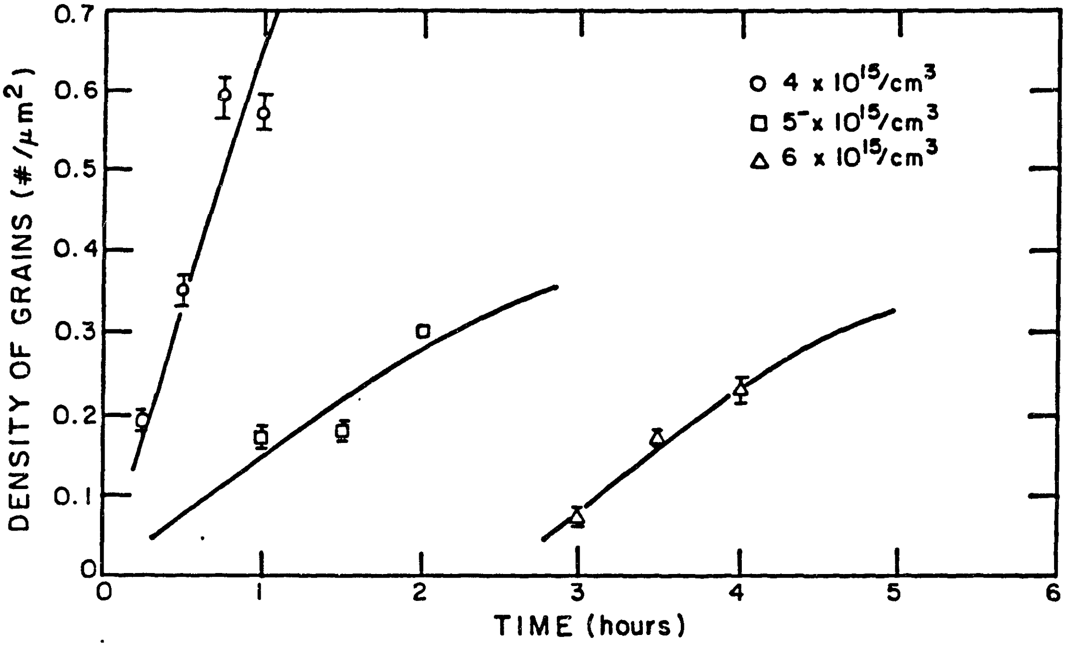

Figure 7.2: Density of grains versus anneal time at 630°C of polycrystalline silicon implanted at 4×10^{15}, 5×10^{15}, and 6×10^{15} ions/cm^2. Each solid line is fit to the data from a given dose by minimizing Eqn. (5.1).

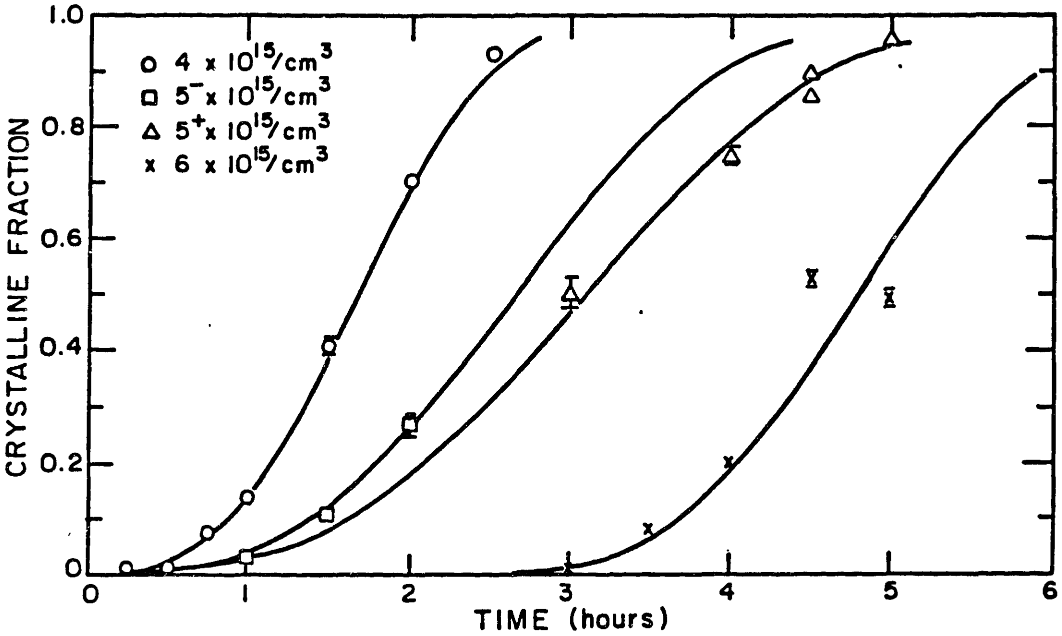

Figure 7.3: Crystalline fraction versus anneal time at 630°C of polycrystalline silicon implanted at 4×10^{15}, 5×10^{15}, and 6×10^{15} ions/cm^2. Each solid line is fit to the data from a given dose by minimizing Eqn. (5.1). The two curves for the "5×10^{15} ions/cm^2" sample are fit to data from different areas of the wafer.

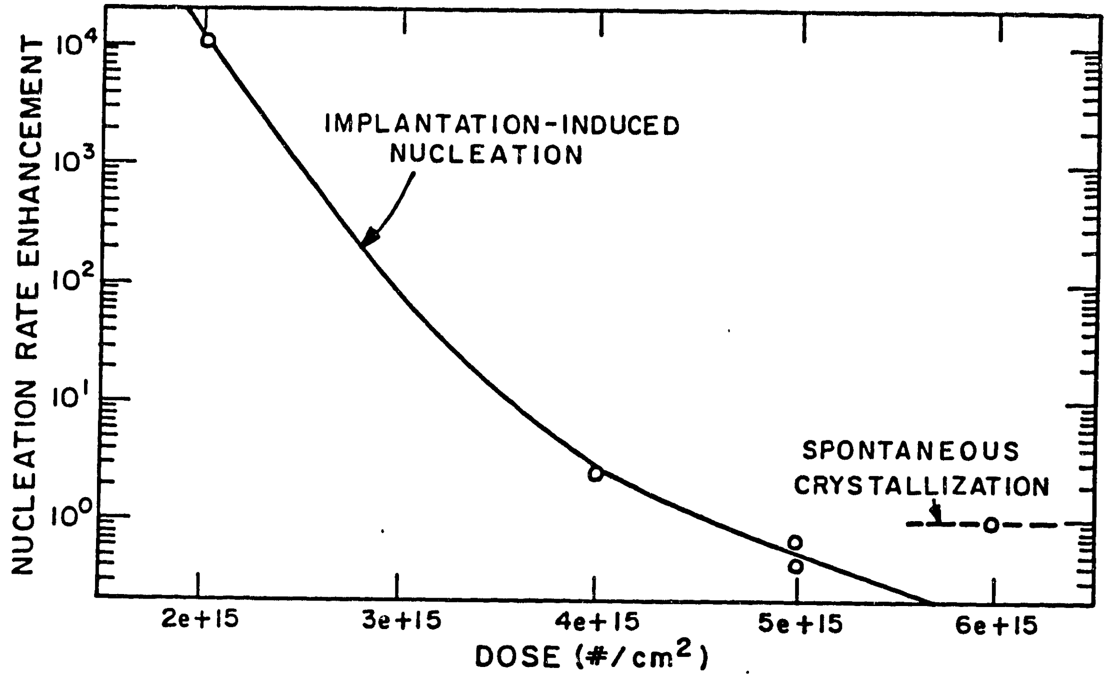

Figure 7.4: Nucleation rate enhancement versus implant dose. Nucleation rates are normalized using the crystallization times found in Chapter 5.

only near the surface (Chapter 6), the film thickness ϵ should be irrelevant. Also, all values of v_g are within 10% of the values found in Chapter 5 for equivalent temperatures.

Using the dose dependence of r_n based on the data points at 4×10^{15} and 5×10^{15} ions/cm^2 in Fig. 7.4, the difference between the "$5^-\times10^{15}$ ions/cm^2" nucleation rate and the "$5^+\times10^{15}$ ions/cm^2" nucleation rate can be attributed to a difference of 3×10^{14} ions/cm^2, or 6% of the implant dose. The wafer-uniformity of the implant is estimated to be 10%.

The extrapolated nucleation rate using Fig. 7.4 at 6×10^{15} ions/cm^2 is so low that during the transient time few grains nucleate and the film will recrystallized due to grains which nucleate after the transient time τ_0.

For a dose of 5×10^{15} ions/cm^2, the initial nucleation rate is less than the steady-state nucleation rate observed in the film implanted at 6×10^{15} ions/cm^2 and the corresponding final grain area A_G is extrapolated to be marginally larger than in the high-dose sample. The grain size at a dose of 5×10^{15} ions/cm^2 is larger than can be attained at either higher or lower doses! At this dose, the nucleation rate (which has been dropping with increasing dose) is lower than the steady-state nucleation rate, but the characteristic time of crystallization τ_n associated with the nucleation rate is on the order of the transient time required to reach steady-state nucleation. For grain-size enhancement, the crystallization time must be smaller than approximately $\tau_0' + \tau_n'$ and larger than τ_n'. (The prime (') indicates values for 100% amorphous material.) When the crystallization is much larger than $\tau_0' + \tau_n'$, steady-state spontaneous nucleation is responsible for much of the crystallization. When the crystallization time is smaller than τ_n', the nucleation rate must be higher than the steady-state spontaneous nucleation rate (for the same growth velocities). Because τ_0' and τ_n' are similar, there is only a very small range of implant doses for which A_G will be larger than in 100% amorphous material. Additionally, the increase in size is marginal. (From Eqn. (B.11), decreasing the nucleation rate by a factor of 2 results in an enhanced grain diameter of $\sqrt[3]{2}$, or a 26% increase.)

7.1.3 As-implanted cluster distribution

A simple model developed in Chapter 2 states that the number N_n of clusters surviving a high-dose implant (2×10^{15} ions/cm^2 or larger) is proportional to $\exp(-C'Qn)$ where C' is a constant, Q is the implant dose, and n

is the cluster size. At sufficiently high doses, virtually no clusters will exist and the material is 100% amorphous.

The nucleation rate is a function of the size-distribution of these clusters (denoted N_n) as well as the total population. In 100% amorphous material (no clusters initially) N_n will evolve with anneal time, approaching a steady-state distribution $N_n(\infty)$. The crystallization behavior of the "5×10^{15} ions/cm^2" film, however, indicates that the size-distribution of clusters attained by implantation is not the same shape that is attained during any stage of an anneal from an initial zero-cluster condition. If this were the case, the crystallization behavior would be the same as if a higher dose were implanted and partly annealed. This fact provides some insight into the as-implanted distribution of cluster sizes.

The sketch in Fig. 7.5 illustrates the evolution of N_n with time. Each solid line represents a snapshot of N_n in material which is initially 100% amorphous. This is analogous to the voltage response in a *variable* transmission line with a step input and a small load resistor. As drawn, the solid lines in Fig. 7.5 indicate a negligible nucleation rate for $t < \tau_0$ and a steady-state nucleation rate thereafter.

Each dashed line represents a snapshot of N_n with an initial distribution of clusters. The dashed lines are drawn to result in a small nucleation rate for $t < \tau_0$ and a steady-state nucleation rate thereafter.

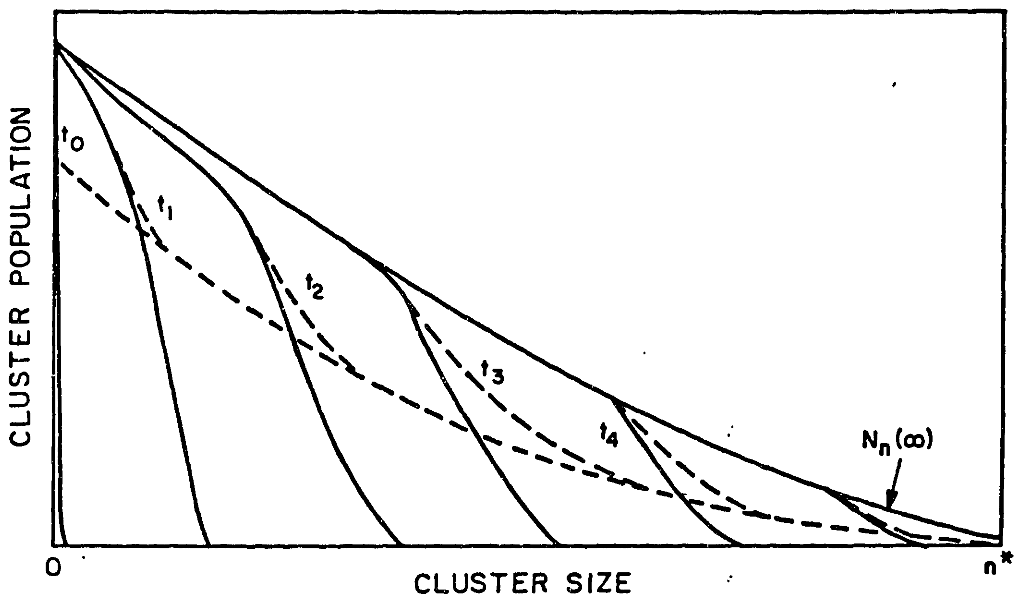

Figure 7.5: Hypothetical time-evolution of the size-distribution of clusters, N_n. The solid lines are for 100% amorphous material (no clusters initially). The dashed lines are for material which is nearly 100% amorphous. In either case, the system approaches the steady-state distribution $N_n(\infty)$

7.2 Summary and Discussion

Three sources of crystallization have been now been identified in self-implanted polycrystalline silicon films: crystallization from seed grains surviving the implant, from microcrystals surviving the implant, and from spontaneously nucleated grains.

Crystallization from seed grains, while hypothesized, has not been demonstrated experimentally by the crystallization behavior of implanted polycrystalline films. Three related experiments by Kung *et al.*[19–21], however, indicated a range of doses which resulted in enhanced {110} texture, presumably due to seed grains which survived the implant due to ion channeling.

Spontaneous crystallization is observed in heavily implanted material and (except for transient time) it is found to be similar to crystallization of silicon films deposited in the amorphous state. The transient time is the time required to reproduce the steady-state cluster population eradicated by implantation and should be observable in implanted amorphous SOI as well.

Implantation-induced nucleation was not foreseen, but is found by experiment in this chapter and in Chapter 6. In hindsight, seeds which survive the implant can be any size. In fact, the distribution of sizes (by *area*) is used as a function (ρ_A) in Appendix A in order to calculate the survival probability of a seed grain. A convenient dividing line between "clusters" and "seed grains" is the critical cluster size n^*. Above a dose of 2×10^{15} ions/cm^2, the number of clusters containing more than n^* atoms is swamped by the number of clusters containing fewer than n^* atoms.

It should be noted that the nucleation rate due to clusters surviving the implant can be time-dependent, according to the size-distribution of the clusters. For the experiments in this thesis, however, a time-independent cluster nucleation rate seems to be a reasonable approximation.

Chapter 8

Conclusions

8.1 Summary

This thesis determines the crystallization behavior in self-implanted polycrystalline SOI films. Polycrystalline silicon films are first deposited on thermally-oxidized silicon wafers by LPCVD and then implanted in order to partly or entirely amorphize the film. The crystallization behavior is investigated by analyzing TEM micrographs of a series of samples annealed isothermally. By measuring grain density χ and crystalline fraction ρ_g versus anneal time, the source of crystallization (seed grains or nucleating crystals) and crystalline growth rate is determined. For growth from nucleating crystals, values for the nucleation rate and (where applicable) the transient time (during which negligible nucleation occurs) are extracted.

The density of seeds in the as-implanted film is estimated from the grain size A_G in 100% recrystallized samples (Chapter 4), taking steady-state spontaneous nucleation of grains into account. A model developed in Chapter 2 and based on an effective damage area A_D conforms well to experiment. Estimating the as-implanted state on basis of the final grain size, however, results in an oversimplified model, as indicated by subsequent experiments.

The crystallization behavior of heavily-implanted films (Chapter 5) is very similar the the crystallization behavior of films which were deposited in the amorphous state.[56,57,58] Crystallization is from grains which nucleate at a steady-state rate r_n. Unlike films deposited in the amorphous state, however, an initial transient time is observed, during which little or no nucleation occurs. This is because the microcrystals which are in amorphous silicon films (deposited above room temperature) are not in heavily-implanted films.

For films with a grain size below the spontaneous-nucleation limit, the final grain size was originally attributed to seed grains, grains which partly survive the implant. However, the crystallization behavior of a "seeded" film (Chapter 6) indicates that crystallization is due to a very high spontaneous nucleation rate, nearly four orders of magnitude larger than in the amorphized film of Chapter 5. Also, cross-sectional TEM indicates that the nucleation occurs at or near the surface.

In view of this phenomenon, three sources of crystallization are now considered in self-implanted polycrystalline silicon films: seed grains surviving the implant, microcrystals surviving the implant, and spontaneously nucleated grains. A seed grain and a microcrystal are both small volumes which by chance (and possibly aided by channeling) survive the implant. The difference between a grain and a microcrystal is the size — seeds are larger than critical cluster size and, therefore, growth is energetically fa-

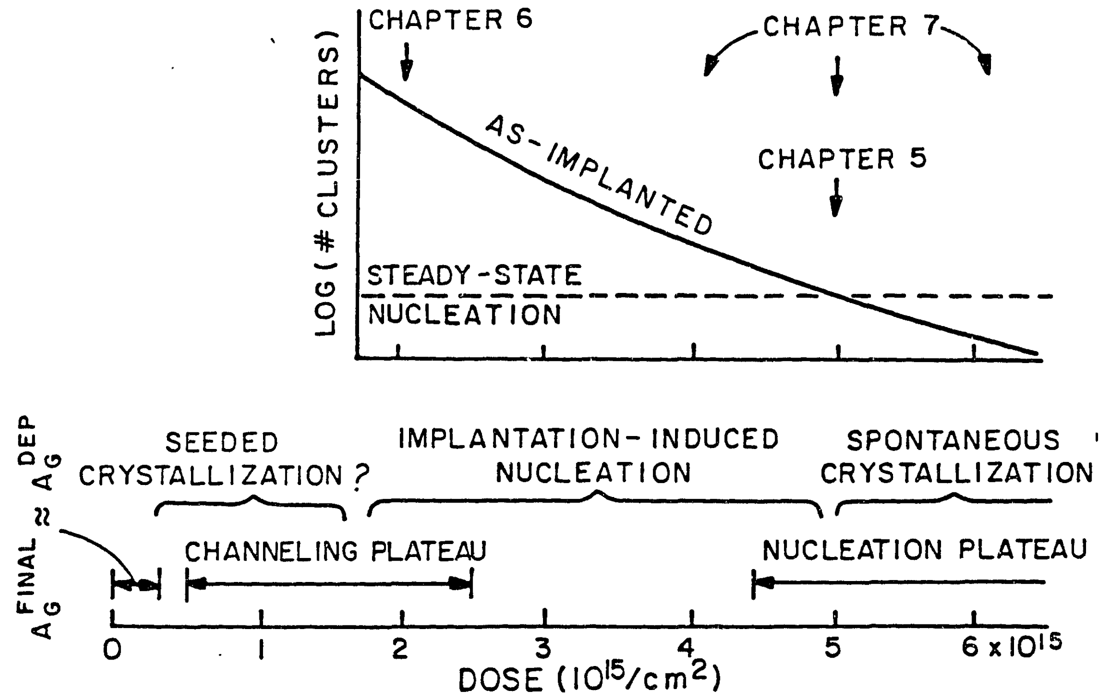

Figure 8.1: Summary of implant effects as a function of dose. Experiments included herein are also shown.

vorable; whereas, microcrystals are smaller than critical cluster size and although growth is *not* energetically favorable a fraction will grow (due to thermodynamics) until further growth becomes favorable, contributing to the nucleation rate. The fraction which becomes "super-critical" is a function of the cluster size n — smaller cluster sizes are more likely to shrink.

The effect of implantation on crystallization behavior is summarized in Fig. 8.1, which also indicates the doses used in the experiments of Chapters 4–7. By implantation, a polycrystalline film becomes amorphous in a fairly complex manner:

- At low implant doses, the film is nearly amorphous, but enough crystalline material is left that a subsequent anneal reproduces the morphology of the as-deposited film.
- As the dose is increased, fewer grains survive and the grains in the implanted and annealed film are larger than in the as-deposited film.
- At still higher doses (the "channeling regime"), only grains which exhibit ion channeling survive; the annealed film has larger grains and is textured as well. Within the channeling regime, the seed size in the as-implanted film decreases with increasing dose until the annealed grain size is determined by an implantation-induced nucleation rate (due to clusters).
- At large doses (complete amorphization) the final grain size saturates at 1–2 μm. The crystallization behavior in this regime indicates that this occurs by a steady-state nucleation rate after a transient time. The transient period is the time necessary to produce a steady-state cluster (microcrystal) population, which is a prerequisite to steady-state nucleation.

Furthermore, over a very small range of doses just before complete amorphization, the implantation-induced nucleation rate is less than the steady-state nucleation rate. Because of the low nucleation rate during the transient time, a small increase in grain size is observed. The grain size can be only marginally enhanced because the transient time τ_0 is roughly the same as the characteristic time of spontaneous nucleation, τ_n. From the results of Chapter 5, τ_0/τ_n is 0.35 at 580°C and rises to 1.05 at 640°C; any process which needs to take advantage of crystal growth during the transient time should produce better results at higher temperatures. This also applies, for example, to solid-phase lateral epitaxial overgrowth from seed windows into an implanted silicon film.

This thesis explains both theoretically and experimentally the crystallization behavior of implanted polycrystalline silicon and provides insights into the structure of as-implanted polycrystalline materials.

8.2 Suggestions for future work

This thesis provides many insights into implantation effects in polycrystalline materials. Several points have been raised which merit future work.

8.2.1 Implant conditions

- Kung *et al.*[19] found that the {110} texture disappeared at an implant angle of 5° from normal incidence. By finding the dose dependence of implanted silicon at this implant angle and comparing the results with those of a 0° implant, the effect of channeling can be quantized.
- The goal of seed selection through ion channeling (SSIC) is to produce uniformly-oriented polycrystalline silicon. To date, only axially-oriented films have been attained. Two approaches may need to be tried:
  - Implant at 0° and 60° and anneal. Previous dose-dependent results cannot be used to find the dose required since damage is

not linear; so, several doses will have to be tried. Furthermore, the relative doses may need to be tailored.

  - Implant at 0° and anneal, and then at 60° and anneal. The first dose should be picked to maximize the {110} texture. The second dose needs to be to determined.

  In either case, the implant energy at 60° must be larger than at 0° since the film is effectively twice as thick.

- The implant-energy dependence of the effective damage area A_D is easily modeled: since the least amount of damage occurs at the surface, where the ion energy is largest, the effective damage area is probably inversely proportional to the average distance between collisions. Experimental confirmation involves finding the dose dependence of final grain size as a function of implant energy.

- The target-temperature dependence of A_D may be difficult to model quantitatively, though it can be found by experiment.

8.2.2 Seeded crystallization

- Seeded crystallization has not been found here. By observing the crystallization behavior of a film implanted at a dose lower than 2×10^{15} ions/cm^2 (used in Chapter 6), perhaps seeded crystallization in implanted films can be documented.

- Through observing the crystallization behavior of seeded films, the final grain size can be accurately determined and compared to the model of final grain size versus implant dose. The "seed density vs.

dose" data may then be correlated with the {110} "texture vs. dose" data.

- Careful examination of TEM diffraction images of individual grains in a partially recrystallized film may indicate the fraction of seeds which are selected due to channeling at an optimal SSIC dose.

8.2.3 Implantation-induced nucleation

- The temperature dependence of implantation-induced nucleation should be investigated. Whether it follows the temperature dependence of the spontaneous nucleation rate is unclear since it is not a steady-state process.
- By observing the crystallization behavior of seeded films, the final grain size can be *accurately* determined for a better comparison to the model of final grain size versus implant dose.
- Implantation-induced nucleation can be investigated theoretically. The size-distribution of clusters surviving the implant can be investigated and the shape of the resulting nucleation transient can then be estimated.
- The experimental dose-dependence of implantation-induced nucleation should investigated more thoroughly. Correlated with "seed density and texture vs. dose" data, this may provide insight into orientation effects by clusters.

8.2.4 Spontaneous nucleation

- Whether the films used in Chapter 5 are completely amorphous has not been determined. This may be checked through crystallization experiments using polycrystalline films implanted at higher doses.
- The source of spontaneous nucleation in silicon has not been found. It may be a bulk property or it may be surface-induced. This can be resolved by measuring the nucleation rate as a function of film thickness.
- The "temperature dependence of the crystallization parameters" results should be extended to a higher temperature. This probably requires rapid thermal annealing because τ_0 and τ_n decrease rapidly with increasing temperature.

8.2.5 Electrical properties

- The electrical properties of implanted and annealed silicon should be correlated with grain size. Larger grains are associated with higher channel mobility and lower conductivity. The large-grain silicon produced by implantation contains many twins and defects which may offset any advantage of large grains.

8.2.6 Silicon-on-insulator technologies

- Solid-phase lateral epitaxial overgrowth experiments may be performed at various temperatures to determine whether the overgrowth distance increases with anneal temperature, as predicted.

- A hot implant of a slightly-recrystallized film may inhibit nucleation while enhancing the growth rate, producing grain sizes larger than 1–2 μm.

Appendix A

Survival Probability of an Implanted Grain

In this appendix, we calculate the probability P_G that a crystalline grain of area A_G survives an implant dose of Q (ions per unit area). The model used here includes the following assumptions:

1. The cascade from a single ion produces some degree of amorphization. The degree of amorphization depends on many factors: implant species, energies, and angles; the target composition; and the target temperature. The amount and shape of the resulting amorphous zone varies from ion to ion and is well beyond the scope of this analysis. The damage produced by an ion, therefore, is approximated here by an average effective damage area A_D, which is some function of the implant parameters.
2. If a grain is not completely amorphized it is assumed to have survived the implant.

3. Amorphization of polycrystalline silicon becomes apparent for doses larger than about 10^{14} ions/cm^2. For a grain size on the order of 100Å, this is equivalent to roughly 100 ions/grain. The equation for P_G, therefore, is simplified assuming $A_D \ll A_G$.
4. Because $A_D \ll A_G$, in the region of interest most of any grain is amorphized.

A.1 Analysis in terms of undamaged-area distribution

The survival probability P_G can be found if the distribution of ***undamaged*** areas is known. This distribution is denoted ρ_A. (The density of undamaged areas between size a_u and $a_u + \Delta a_u$ is $\rho_A(a_u)\Delta a_u$.) In the region of interest, the density of undamaged areas should be small (because $A_D \ll A_G$). The positions of the undamaged areas, therefore, can be considered random and uncorrelated. This condition implies that the probability that a grain is completely amorphized $(1 - P_G)$ is the product of the probabilities that the area of the grain does not overlap any undamaged areas for all sizes of undamaged areas. Consider a single undamaged region of area a_u. The area over which this region could be located to intersect a given grain is written here as

$$A_G{}'(a_u) = a_u + 2C\sqrt{a_u A_G} + A_G, \tag{A.1}$$

where C depends on the shapes of A_G and a_u. If both shapes are convex and similar but one is rotated by 180° then $C = 1$. For sample area A_∞, the survival probability is

$$(1 - P_G) = \prod_{i=0}^{\infty} \left(1 - \frac{A_G{}'(i\Delta a_u)}{A_\infty}\right)^{A_\infty \rho_A(i\Delta a_u)\Delta a_u}, \tag{A.2}$$

where Δa_u is an incremental area. The product in Eqn. (A.2) can be changed to a summation by taking the natural logarithm of each side. Furthermore, for a large sample area, the sum can be replaced by an integral and the integrand is easily simplified:

$$\begin{aligned}
\ln(1 - P_G) &= \ln\left[\prod_{i=0}^{\infty} \left(1 - \frac{A_G{}'(i\Delta a_u)}{A_\infty}\right)^{A_\infty \rho_A(i\Delta a_u)\Delta a_u}\right] \\
&= \sum_{i=0}^{\infty} \ln\left(1 - \frac{A_G{}'(i\Delta a_u)}{A_\infty}\right) A_\infty \rho_A(i\Delta a_u)\Delta a_u \\
&= \int_0^\infty \ln\left(1 - \frac{A_G{}'(a_u)}{A_\infty}\right) A_\infty \rho_A(a_u) \mathrm{d}a_u \\
&= -\int_0^\infty A_G{}'(a_u)\rho_A(a_u)\mathrm{d}a_u \\
&= -\int_0^\infty (a_u + 2C\sqrt{a_u A_G} + A_G)\rho_A(a_u)\mathrm{d}a_u
\end{aligned} \tag{A.3}$$

A.2 Virtual undamaged-area fraction

The undamaged-area distribution ρ_A can also be related to the *virtual* undamaged-area fraction $f_A(a_d)$, which is the fraction of the sample not within area a_d of any impact position. The parameter a_d can be considered to be a virtual damage area. Since the impact positions are random and uncorrelated, f_A is the product of the probabilities that a point is not within area a_d of each impact position. In a large sample ($A_\infty \to \infty$),

$$\begin{aligned}
f_A(a_d) &= \left(1 - \frac{a_d}{A_\infty}\right)^{QA_\infty} \\
&= \exp(-Qa_d).
\end{aligned} \tag{A.4}$$

Note that the amorphized fraction is $f_A(A_D) = \exp(-QA_D)$.

For $a_d > A_D$, f_A can be related to the distribution of undamaged regions. Specifically, an undamaged area a_u includes an area $a_u{}'$ which is not within an area a_d of any impact position. (For example, the area $a_u{}'$ would be the same as a_u if a_d were the same as A_D). Assuming the area of a region is proportional to the square of its radius, the incremental contribution to $f_A(a_d)$ by undamaged regions of areas a_u to $a_u + \Delta a_u$ is

$$\Delta f_A = \left\{ \frac{\left[\sqrt{a_u} - \left(\sqrt{a_d} - \sqrt{A_D}\right)\right]^2}{A_\infty} \right\} \left\{ A_\infty \rho_A(a_u) \Delta a_u \right\}. \qquad \text{(A.5)}$$

The first term in Eqn. (A.5) is the contribution from each region. The second term is the number of such regions in the sample.

By integration of Eqn. (A.5) over the appropriate limits, the undamaged-area distribution ρ_A can be related to the virtual undamaged-area fraction:

$$f_A(a_d) = \int_{a_{u,min}}^{\infty} \left(\sqrt{a_u} - \sqrt{a_d} + \sqrt{A_D}\right)^2 \rho_A(a_u) \mathrm{d}a_u, \qquad \text{(A.6)}$$

where $a_{u,min}$ is given by

$$a_{u,min} = \left(\sqrt{a_d} - \sqrt{A_D}\right)^2 \qquad \text{(A.7)}$$

Substitution of Eqn. (A.4) into Eqn. (A.6) gives

$$\exp(-Qa_d) = \int_{a_{u,min}}^{\infty} \left(\sqrt{a_u} - \sqrt{a_d} + \sqrt{A_D}\right)^2 \rho_A(a_u) \mathrm{d}a_u. \qquad \text{(A.8)}$$

A.3 Survival probability

A formula for P_G can be found from Eqns. (A.3) and (A.8) using the following substitutions:

$$\begin{aligned}
A_G &\rightarrow R_G^2 \\
A_D &\rightarrow R_D^2 \\
a_u &\rightarrow r_u^2 \\
a_d &\rightarrow r_d^2 \\
a_{u,min} &\rightarrow r_{u,min} \\
\rho_A(a_u)\mathrm{d}a_u &\rightarrow \rho_R(r_u)\mathrm{d}r_u
\end{aligned} \tag{A.9}$$

Equation (A.3) becomes

$$-\ln(1-P_G) = \int_0^\infty (r_u^2 + 2Cr_uR_G + R_G^2)\rho_R(r_u)\mathrm{d}r_u. \tag{A.10}$$

Equation (A.8) becomes

$$\exp(-Qr_d^2) = \int_{r_{u,min}}^\infty (r_u - r_d + R_D)^2 \rho_R(r_u)\mathrm{d}r_u. \tag{A.11}$$

When $r_d = R_D$, the lower limit is $r_{u,min} = 0$ and Eqn. (A.11) becomes

$$\exp(-QR_D^2) = \int_0^\infty r_u^2\rho_R(r_u)\mathrm{d}r_u. \tag{A.12}$$

Note that the first term in the integral in Eqn. (A.10) is the same as the right-hand side of Eqn. (A.12).

The derivative of Eqn. (A.11) with respect to r_d is

$$-2Qr_d\exp(-Qr_d^2) = \int_{r_{u,min}}^\infty -2(r_u - r_d + R_D)\rho_R(r_u)\mathrm{d}r_u. \tag{A.13}$$

When $r_d = R_D$, the lower limit is $r_{u,min} = 0$ and Eqn. (A.13) becomes

$$-2QR_D \exp\left(-QR_D^2\right) = \int_0^\infty -2r_u\rho_R(r_u)\mathrm{d}r_u. \tag{A.14}$$

Note that the second term in the integral in Eqn. (A.10) is the same as the right-hand side of Eqn. (A.14) weighted by $-CR_G$

The derivative of Eqn. (A.13) with respect to r_d is

$$\left(-2Q + 4Q^2r_d^2\right)\exp\left(-Qr_d^2\right) = \int_{r_{u,min}}^\infty 2\rho_R(r_u)\mathrm{d}r_u. \tag{A.15}$$

When $r_d = R_D$, the lower limit is $r_{u,min} = 0$ and Eqn. (A.15) becomes

$$\left(-2Q + 4Q^2R_D^2\right)\exp\left(-QR_D^2\right) = \int_0^\infty 2r_u\rho_R(r_u)\mathrm{d}r_u. \tag{A.16}$$

Note that the third term in the integral in Eqn. (A.10) is the same as the right-hand side of Eqn. (A.16) weighted by $R_G^2/2$

Substituting Eqns. (A.12), (A.14), and (A.16) into Eqn. (A.10) gives

$$\begin{aligned} -\ln\left(1 - P_G\right) &= \exp\left(-QR_D^2\right) + 2CQR_GR_D\exp\left(-QR_D^2\right) \\ &\quad + \left(2Q^2R_G^2R_D^2 - QR_G^2\right)\exp\left(-QR_D^2\right) \\ &= \left(1 + 2CQR_GR_D + 2Q^2R_G^2R_D^2 - QR_G^2\right) \\ &\quad \times\exp\left(-QR_D^2\right) \end{aligned} \tag{A.17}$$

Resolving the substitutions of Eqn. (A.9) yields

$$\begin{aligned} -\ln\left(1 - P_G\right) &= \left(1 + 2CQ\sqrt{A_GA_D} + 2Q^2A_GA_D - QA_G\right) \\ &\quad \times\exp\left(-QA_D\right) \end{aligned} \tag{A.18}$$

Because $A_G \gg A_D$ and the geometrical factor C is on the order of 1, the fourth term dominates the second; hence,

$$-\ln\left(1 - P_G\right) \approx \left(1 + 2Q^2A_GA_D - QA_G\right)\exp\left(-QA_D\right) \tag{A.19}$$

A.4 Range of validity

Since P_G monotonically decreases with dose, $(1 - P_G)$ monotonically increases, and both sides of Eqn. (A.19) must monotonically decrease. The derivative (set to zero) is

$$\begin{aligned} 0 &= -A_D\left(1 + 2Q^2 A_G A_D - QA_G\right) + (4QA_G A_D - A_G) \\ &= Q^2(A_G {A_D}^2) - Q(5A_G A_D) + (A_G + A_D) \\ &\approx (QA_D)^2 - 5(QA_D) + 1. \end{aligned} \tag{A.20}$$

A lower bound to the valid range of the doses is found by the solutions of Eqn. (A.20): $QA_D > 4.6$; the smallest dose for which the model is valid would amorphize the sample 4.6 times if the impact positions were uniform! Since $QA_G \gg QA_D > 4.6$, Eqn. (A.19) can be simplified further:

$$beginequation - \ln(1 - P_G) \approx 2Q^2 A_G A_D \exp(-QA_D). \tag{A.21}$$

Appendix B

Spontaneous Crystallization

In this appendix, we calculate the crystalline fraction $\chi_n(t)$, the density of grains $\rho_n(t)$, and final grain size $A_{G,n}$ due to growth of crystallites which nucleate at a steady-state rate r_n in an amorphous film of thickness ϵ. We assume that the grains grow anisotropically with a steady-state growth velocity v_g and that impinging grains can be treated by superposition (though no crystalline area will be tallied twice). The film is considered in two dimensions only — the nucleation rate (per unit area) is ϵr_n.

B.1 Crystalline fraction

Within a large sample area A_∞, the first nucleation event can be considerer to occur at time $t_1 = 1/\epsilon r_n A_\infty$. At a later time t, the amorphous fraction $[1 - \chi_n(t)]$ due to this grain is

$$[1 - \chi_n(t)] = \left[1 - \frac{\pi {v_g}^2 (t - t_1)^2}{A_\infty}\right] \tag{B.1}$$

Similarly, the second nucleation event can be considered to occur at time $t_2 = 2/\epsilon r_n A_\infty$. This will only occur with probability $[1 - \chi_n(t_2)]$.

Mathematically, however, the possibility of a grain nucleating within a crystalline area may be allowed — the crystalline fraction is not changed by such a "virtual" grain since its growth front cannot overtake the growth front of the grain it has nucleated in. In other words, we consider that the second nucleation event (which may be virtual) is totally independent of the first. Similarly, we can consider each grain to have a virtual area of $\pi v_g{}^2(t - t_i)^2$, independent of possible overlap. Because the nucleation events are independent, the amorphous fraction after the second event is the product of two probabilities: the probability that a randomly selected point is not within the virtual area of the first grain, and the probability that the selected point is not within the virtual area of the second grain.

$$[1 - \chi_n(t)] = \left[1 - \frac{\pi v_g{}^2(t - t_1)^2}{A_\infty}\right]\left[1 - \frac{\pi v_g{}^2(t - t_2)^2}{A_\infty}\right]. \tag{B.2}$$

This approach may be extended to any time t, at which there will have been a total of $\epsilon r_n A_\infty t$ nucleation events, virtual and real:

$$[1 - \chi_n(t)] = \prod_{i=1}^{\epsilon r_n A_\infty t}\left[1 - \frac{\pi v_g{}^2(t - t_i)^2}{A_\infty}\right]. \tag{B.3}$$

Solving Eqn. (B.3) involves changing the product over the grains to a sum by taking the logarithm and changing the sum over the grains to an integral over time, realizing that within $\mathrm{d}t'$, the number of nucleation events that occur (virtual and real) is $\epsilon r_n A_\infty \mathrm{d}t'$:

$$\begin{aligned} \ln[1 - \chi_n(t)] &= \ln\left\{\prod_{i=1}^{\epsilon r_n A_\infty t}\left[1 - \frac{\pi v_g{}^2(t - t_i)^2}{A_\infty}\right]\right\} \\ &= \sum_{i=1}^{\epsilon r_n A_\infty t} \ln\left[1 - \frac{\pi v_g{}^2(t - ti)^2}{A_\infty}\right] \end{aligned}$$

$$= \int_0^t \ln\left[1 - \frac{\pi {v_g}^2 (t-t')^2}{A_\infty}\right] \epsilon r_n A_\infty \mathrm{d}t'. \tag{B.4}$$

For a large sample area, the integrand in Eqn. (B.4) may be expanded:

$$\begin{aligned} \ln\left[1 - \chi_n(t)\right] &= -\int_0^t \pi {v_g}^2 (t-t')^2 \epsilon r_n \mathrm{d}t' \\ &= -\frac{\pi}{3} {v_g}^2 \epsilon r_n t^3. \end{aligned} \tag{B.5}$$

Equation (B.5) is usually written in the form

$$x_n(t) = 1 - \exp\left[-(t/\tau_n)^3\right] \tag{B.6}$$

where τ_n is the characteristic crystallization time due to a steady-state nucleation rate:

$$\tau_n = 1/\sqrt[3]{\tfrac{\pi}{3} {v_g}^2 \epsilon r_n} \tag{B.7}$$

B.2 Density of grains

Once the crystalline fraction is known, the density of nucleated grains ρ_n is easily calculated from the effective nucleation rate, which is $\epsilon r_n[1 - x_n(t)]$:

$$\begin{aligned} \rho_n(t) &= \int_0^t \epsilon r_n \left[1 - \chi(t')\right] \mathrm{d}t' \\ &= \epsilon r_n \tau_n \int_0^u \exp(-u'^3) \mathrm{d}u'. \end{aligned} \tag{B.8}$$

where u is normalized crystallization time, t/τ_n. The integral in Eqn. (B.8) is unitless and depends only on normalized time. It is abbreviated $g(u)$:

$$g(u) = \int_0^u \exp(-u'^3) \mathrm{d}u'. \tag{B.9}$$

Substituting Eqn. (B.9) into Eqn. (B.8) gives

$$\rho_n(t) = \epsilon r_n \tau_n \, g(u). \tag{B.10}$$

B.3 Final grain size

The final grain size due to nucleation alone $A_{G,n}$ is the inverse of the final grain density $\rho_n(\infty)$. From Eqn. (B.9), $g(\infty) = \Gamma\left(\frac{4}{3}\right)$; so, the final grain size is

$$\begin{aligned} A_{G,n} &= \left[\epsilon r_n \tau_n \, \Gamma\left(\tfrac{4}{3}\right)\right]^{-1} \\ &= \frac{\sqrt[3]{\pi/3}}{\Gamma\left(\frac{4}{3}\right)} \left(\frac{v_g}{\epsilon r_n}\right)^{2/3} \end{aligned} \tag{B.11}$$

Appendix C

Seeded Crystallization

In this appendix, we calculate the crystalline fraction $\chi_s(t)$ due to crystallization from an initial density of seed grains, ρ_s.

As in the analysis of spontaneous crystallization (Appendix B), we assume that the grains grow anisotropically with a steady-state growth velocity v_g and that impinging grains can be treated by superposition of their virtual areas. Furthermore, the areas of the seed crystals are neglected, which is valid when the sample is nearly 100% amorphous initially.

At time t, the virtual area of each grain is

$$A_G(t) = \pi {v_g}^2 t^2. \tag{C.1}$$

The amorphous fraction is the probability that a randomly-selected point is not within the area of any grain. By allowing the circular grains to be superimposed, the effect of each grain is independent so that the amorphous fraction is the product of the individual probabilities. In a sample of area A_∞, the number of grains is $A_\infty \rho_s$ and the amorphous fraction is given by

$$[1 - \chi_s(t)] = \left[1 - \frac{\pi {v_g}^2 t^2}{A_\infty}\right]^{A_\infty \rho_s} \tag{C.2}$$

For a large sample area, the right side of Eqn. (C.2) reduces to

$$[1-\chi_s(t)] = \exp\left[-\pi {v_g}^2 \rho_s t^2\right] \tag{C.3}$$

Equation (C.3) is usually written

$$\chi_s(t) = 1 - \exp\left[-(t/\tau_s)^2\right], \tag{C.4}$$

where τ_s is the characteristic time of crystallization due to seed grains alone:

$$\tau_s = 1/\sqrt{\pi {v_g}^2 \rho_s}. \tag{C.5}$$

References

[1] A. Gat, L. Gerzberg, J. F. Gibbons, T. J. Magee, J. Peng, and J. D. Hong, *Appl. Phys. Lett.* **33**, 775 (1978).

[2] G. K. Celler, McD. Robinson, and D. J. Lischner, *Appl. Phys. Lett.* **42**, 99 (1983).

[3] M. W. Geis, D. C. Flanders, and Henry I. Smith, *Appl. Phys. Lett.* **35**, 71 (1979).

[4] M. W. Geis, D. A. Antoniadis, D. J. Silversmith, R. W. Mountain, and Henry. I. Smith, *Appl. Phys. Lett.* **37**, 454 (1980).

[5] H. Ishiwara, H. Yamamoto, and S. Furukawa *Appl. Phys. Lett.* **43**, 1028 (1983).

[6] H. Yamamoto, H. Ishiwara, and S. Furukawa *Appl. Phys. Lett.* **46**, 268 (1985).

[7] P. Kwizera and R. Reif, *Appl. Phys. Lett.* **33**, 775 (1978).

[8] R. Reif and J. E. Knott, *Electron. Lett.* **17**, 586 (1981).

[9] C. V. Thompson, *Appl. Phys. Lett.* **44**, 603 (1984).

[10]E. Chartier, N. Szydlo, F. Boulitrop, N. Proust, and J. Magarino, *Mat. Res. Symp. Proc.* **53**, 453 (1986).

[11]S. Malhi, H. Shichijo, S. Banerjee, R. Sundaresan, M. Elahy, G. Pollack, W. Richardson, A. Shah, L. Hite, R. Womack, P. Chatterjee, and H. Lam, *IEEE J. Solid-State Circuits* **20**, 178 (1985).

[12]T. Ohshima, T. Noguchi, and H. Hayashi, *Jap. J. Appl. Phys.* **25** L291 (1986).

[13]T. I. Kamins, *J. Elchem. Soc.* **127**, 686 (1980).

[14]M. Rodder, D. A. Antoniadis, F. Scholz, A. Kalnitsky, *IEEE Elec. Dev. Lett.* **8**, 27 (1987).

[15]Y. Komem and I. W. Hall, *J. Appl. Phys.* **52**, 6655 (1981).

[16]R. B. Iverson, and R. Reif, *Mat. Res. Symp. Proc.* **27**, 543 (1984).

[17]R. S. Nelson and D. M. Mazey, *J. Mat. Sci.* **2**, 211 (1967).

[18]R. B. Iverson, and R. Reif, *J. Appl. Phys.* **57**, 5169 (1985).

[19]K. T-Y. Kung, R. B. Iverson, and R. Reif, *Mat. Lett.* **3**, 24 (1984).

[20]K. T-Y. Kung, R. B. Iverson, and R. Reif, *Appl. Phys. Lett.* **46**, 683 (1985).

[21]K. T-Y. Kung and R. Reif, *J. Appl. Phys.* **59**, 2422 (1986).

[22]R. B. Iverson and R. Reif, Submitted to *Mat. Lett.*

[23]R. B. Iverson and R. Reif, Submitted to *J. Appl. Phys.*

[24]R. B. Iverson and R. Reif, Submitted to *Appl. Phys. Lett.*

[25]W. Rothemund and C. R. Fritzsche, *Appl. Phys.* **10**, 111 (1976).

[26]M. Huez, F. Cappellani, and G. Restelli, *Rad. Eff.* **32**, 147 (1977).

[27]C. R. Fritzsche and W. Rothemund, *Appl. Phys.* **16**, 339 (1978).

[28]G. K. Hubler, C. N. Waddell, W. G. Spitzer, J. E. Fredrickson, S. Prussin, and R. G. Wilson, *J. Appl. Phys.* **50**, 3294 (1979).

[29]J. Bourgoin, *Sol. State Comm.* **34**, 25 (1980).

[30]G. Muller and S. Kalbitzer, *Phil. Mag. B* **41**, 307 (1980).

[31]T. Ohner, G. Mezey, E. Kotai, F. Paszti, L. Kiralyhidi, G. Valyi, and J. Gyulai, *Nucl. Instrum. Methods* **182/183**, 591 (1981).

[32]J. Narayan, D. Fathy, O. S. Oen, and O. W. Holland, *J. Vac. Sci. Tech.* **2**, 1303 (1984).

[33]W. A. Johnson, and R. F. Mehl, *Trans. Am. Inst. Min. (Metall.) Engrs.* **135**, 416 (1939).

[34]M. Avrami, *J. Chem. Phys.* **7**, 1103 (1939).

[35]M. Avrami, *J. Chem. Phys.* **8**, 212 (1940).

[36]M. Avrami, *J. Chem. Phys.* **9**, 177 (1941).

[37]D. K. Brice, *Rad. Eff.* **6**, 77 (1970).

[38]D. K. Brice, *J. Appl. Phys.* **46**, 3385 (1975).

[39]C. Jech, *Phys. Stat. Sol. A* **3**, 579 (1970).

[40]C. Jech, *Phys. Lett.* **39A**, 417 (1972).

[41]H. Grahmann, A. Feuerstein, and S. Kalbitzer, *Rad. Eff.* **29**, **117** **(1976)**.

[42]D. R. Myers and R. G. Wilson, *Rad. Eff.* **47**, 91 (1980).

[43]J. F. Ziegler and R. F. Lever, *Appl. Phys. Lett.* **46**, 358 (1985).

[44]F. Cembali and F. Zignani, *Rad. Eff.* **31**, 169 (1977).

[45]F. Cembali, L. Dori, R. Galloni, and M. Servidori, *Rad. Eff.* **36**, **111** (1978).

[46]M. L. Swanson, P. Offermann, and K. H. Ecker, *Can. J. Phys.* **57**, **457** (1979).

[47]T. E. Seidel, *Appl. Phys. Lett.* **36**, 447 (1980).

[48]R. Reif and J. E. Knott, *Electron. Lett.* **17**, 586 (1981).

[49]K. F. Kelton, A. L. Greer, and C. V. Thompson, *J. Chem. Phys.* **79**, 6261 (1983).

[50] H. Wakeshima, *J. Chem. Phys.* **22**, 1614 (1954).

[51]F. C. Collins, *Z. Electrochem.* **59**, 404 (1955).

[52]J. Feder, K. C. Russell, J. Lothe, and G. M. Pound, *Adv. Phys.* **15**, 111 (1966).

[53]B. K. Chakraverty, *Surf. Sci.* **4**, 205 (1966).

[54]D. Kashchiev, *Surf. Sci.* **14**, 209 (1969).

[55]J. F. Gibbons, W. S. Johnson, and S. W. Mylroie, Projected range statistics: semiconductors and related materials, 2nd ed., Dowden, Hutchinson, and Ross, Inc. (1975).

[56]. Zellama, P. Germain, S. Squelard, and J. C. Bourgoin, *J. Appl. Phys.* **50**, 6995 (1979).

[57]U. Koster, *Phys. Stat. Sol. A* **48**, 313 (1978).

[58]N. A. Blum and C. Feldman, *J. Non-Cryst. Sol.* **11**, 242 (1972).

[59]L. Csepregi, E. F. Kennedy, and J. W. Mayer, *J. Appl. Phys.* **49**, 3906 (1978).

[60]J. E. Fredrickson, C. N. Waddell, W. G. Spitzer, and G. K. Hubler, *Appl. Phys. Lett.* **40**, 172 (1982).

[61]G. K. Hubler, C. N. Waddell, W. G. Spitzer, J. E. Fredrickson, and T. A. Kennedy, *Mat. Res. Symp. Proc.* **27**, 217 (1984).

[62]R. P. Vasquez, A. Madhukar, and A. R. Tangua, Jr., *J. Appl. Phys.* **58**, 2337 (1985).

[63]I. Golecki, G. E. Chapman, S. S. Lau, B. Y. Tsaur, and J. W. Mayer, *Phys. Lett.* **71A**, 267 (1979).